Aerospace Science and Technology 180 (2027) 114126

Contents lists available at ScienceDirect

Aerospace Science and Technology

journal homepage: www.elsevier.com/locate/aescte

Original article

Experimental investigation of vortex ring state for multicopters

Giosuè Longobardo [a,*], Alexander Heintz [b], Johannes Braukmann [b], C. Christian Wolf [b], Jochen Raddatz [c], Tommaso Astarita [a], Fabrizio De Gregorio [d], Anthony D. Gardner [b], Markus Raffel [b]

[a] University of Naples Federico II, Department of Industrial Engineering, Piazzale Tecchio 80, Naples, 80125, Italy
[b] German Aerospace Center (DLR), Institute of Aerodynamics and Flow Technology, Bunsenstrasse 10, Göttingen, 37073, Germany
[c] German Aerospace Center (DLR), Institute of Aerodynamics and Flow Technology, Lilienthalplatz 7, Braunschweig, 38108, Germany
[d] Italian Aerospace Research Centre (CIRA), Aerodynamic Measurement Methodologies Laboratory, Via Maiorise, Capua (CE), 81043, Italy

ARTICLE INFO

Communicated by Qu Qiulin

Keywords:
VRS
Multicopters
Stereoscopic PIV
Rotor aerodynamics
Urban air mobility

ABSTRACT

The vortex ring state (VRS) regime for multicopters has been experimentally investigated within "GARTEUR AG28: Vortex Ring State" via thrust and power measurements as well as stereo particle image velocimetry (S-PIV), at descent angles between 40° and 90°, and normalised descent rates between −0.4 and −1.7, covering the whole area of flight susceptible to VRS, with the aim of investigating the interaction effects on multirotor configurations in VRS and the deviation of their performance from existing experimental data for conventional helicopters. Four different configurations have been investigated: the single rotor (SR), used as a reference test case, the dual rotors in side-by-side (DRSbS) and tandem (DRT) arrangement and the quadrotor (QR) configuration. Thrust data and S-PIV velocity fields show that while multirotor configurations exhibit qualitative similarities to helicopters in their VRS behaviour, they proved more susceptible to VRS: based on mean thrust reduction, the multirotor configurations show broader regions of the flight envelope affected by VRS compared to the SR configuration. However, similar mean thrust reduction levels are obtained for all configurations, with the highest reduction measured at roughly 25-30%. Significant configurational effects are also found regarding rotor placement, with the DRT and QR configurations showing reduced thrust levels for the rear rotor at shallow descent angles. The QR configuration also showed the highest thrust fluctuations, growing by a factor of 2 compared to the SR configuration. The velocimetry measurements proved that, for the QR configuration, a single recirculation region wraps around the device when in VRS, forming a unified vortex ring. Additionally, the minimum thrust experienced by the configuration is found to correlate with the centre of the recirculation regions being approximately positioned at 1/2 of the device characteristic length from the rotor plane.

1. Introduction

A rotorcraft performing aggressive descent manoeuvres may enter a potentially dangerous flight condition, termed vortex ring state (VRS). VRS arises when the descent rate of the vehicle becomes comparable to the induced velocity of the rotor at the rotor plane, as sketched in Fig. 1b. Phenomenologically, VRS is characterised by reduced thrust, increased thrust fluctuations and vibrations, significant loss of control authority and insurgence of stability issues.

VRS is also characterised by a notable modification in the flow topology: the rotor ingests its wake, and the flow field is dominated by an annular vortex positioned around the rotor plane. This change in flow topology renders low-order methods based on momentum theory inapplicable, as a well-defined slipstream through the rotor disc is no longer present. As a result, flight tests and wind tunnel experiments become essential for understanding and predicting the physics of VRS.

The pioneering works of Reeder and Gustafson [2], Drees and Hendal [3], Castles and Gray [4], Gessow [5], Yeates [6], Yaggy and Mort [7], Washizu et al. [8] and Azuma and Obata [9] already touched upon the most critical issues of VRS.

Most notably, Castles and Gray [4] already discussed the progressive deterioration of a helicopter's attitude control as it enters various stages of VRS, measured via flight tests. They reported on the insurgence of violent yawing/rolling coupled motions and a sudden increase in the vehicle's descent rate.

Gessow [5] focused on the non-dimensional characteristic curves, and proved the intrinsically unstable nature of flight in VRS, noting that the slope of the non-dimensional power plotted against non-dimensional

* Corresponding author.
E-mail address: giosue.longobardo@unina.it (G. Longobardo).

https://doi.org/10.1016/j.ast.2026.114126
Received 4 May 2026; Received in revised form 20 September 2026; Accepted 21 October 2026
Available online 28 October 2026
1270-9638/© 2026 The Author(s). Published by Elsevier Masson SAS. This is an open access article under the CC BY license (http://creativecommons.org/licenses/by/4.0/).

Nomenclature

Acronyms

CMOS	Complementary Metal-Oxide-Semiconductor
CoR	Centre of Rotation
DEHS	Di-Ethyl-Hexyl-Sebacate
DC	Direct Current
DLR	German Aerospace Centre
DRSbS	Dual Rotor in Side-by-Side configuration
DRT	Dual Rotor in Tandem configuration
eROI	extended Region Of Interest
eVTOL	electric Vertical Take-Off and Landing
FOV	Field Of View
FPP	Flight Path Plane
Nd:YAG	Neodymium-doped Yttrium Aluminium Garnet
PSD	Power Spectral Density
QR	Quadrotor Configuration
RTG	Rotor Test facility Göttingen
ROI	Region Of Interest
RMS	Root Mean Square
RPM	Revolutions Per Minute
S-PIV	Stereo Particle Image Velocimetry
SR	isolated Single Rotor configuration
UAM	Urban Air Mobility
UPM	Unsteady Panel Method
VRS	Vortex Ring State
TWS	Turbulent Wake State

Greek Letters

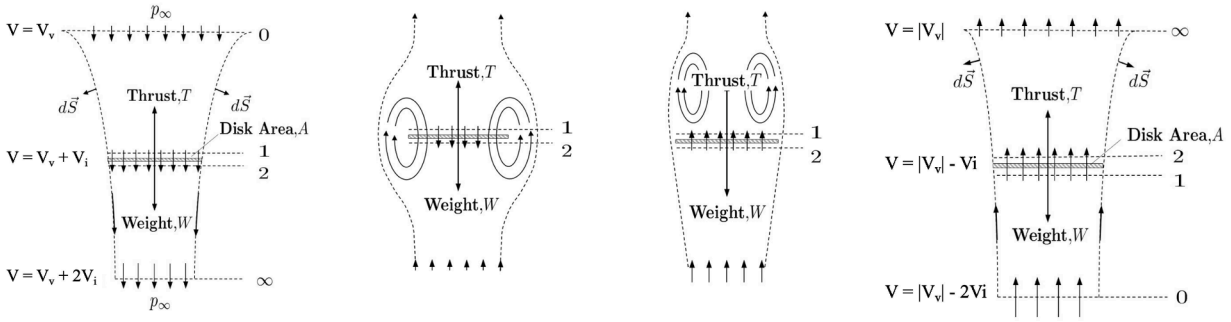
α	descent angle, deg
ΔT	thrust fluctuations, N
ρ	air density, kg/m^3
σ	rotor solidity, dimensionless
ω	characteristic frequency, Hz
ω_{VRS}	reference frequency in VRS, Hz
Ω	rotor angular velocity, rad/s

Non-dimensional numbers

$Re_D = \frac{U_\infty D}{\nu}$	diameter's Reynolds number

Roman Letters

A	rotor disc area, m^2
C_d	sectional drag coefficient, dimensionless
d	rotor separation distance, m
D	rotor diameter, m
DL	disc loading, N/m^2
f	frequency, Hz
P	total required mechanical power, kW
P_0	profile power, kW
P_{ref}	total mechanical power required in hover, kW
R	rotor radius, m
T	mean thrust averaged across the sample, N
$T_{hov.}$	thrust in hover, N
$T_{inst.}$	low-pass filtered instantaneous thrust, N
$T_{\max}$	maximum thrust measured in the sample, N
U	streamwise velocity component, m/s
U_∞	wind tunnel velocity, m/s
V	crosswise velocity component, m/s
V_h	horizontal velocity, m/s
$V_{hov.}$	velocity scale computed in hover, m/
V_i	rotor's induced velocity, m/s
$V_{ref.}$	velocity scale, m/
V_{tip}	tip speed, m/s
V_v	vertical velocity, m/s
X	streamwise coordinate, m
Y	crosswise coordinate, m
W	out-of-plane velocity component, m/s
Z	out-of-plane coordinate, m



(a) Normal Working State, $V_v > 0$. (b) Vortex Ring State, $V_v + V_i > 0$. (c) Turbulent Wake State, $V_v + V_i < 0$. (d) Windmill Brake State, $V_v - 2V_i < 0$.

Fig. 1. Sketches of different flow topologies around a rotor for varying descent rates. Adapted from Veismann et al. [1].

descent velocity is negative. Indeed, for a given rotor pitch, an increase in descent rate causes an increase in induced velocity, or, equivalently, an increase in required power, leading to a further increase in the descent rate.

Washizu et al. [8] and Azuma and Obata [9] focused on the unsteady aerodynamics of VRS by investigating the time histories of thrust, torque and angular velocity of a model helicopter via wind-tunnel tests. The experimental campaign identified significant thrust fluctuations during the onset of VRS, with variations reaching approximately 30% of the mean thrust values. Moreover, a power spectral density analysis revealed that in VRS, significant periodic components are observable in the thrust fluctuations. Beginning in the late 1980s, the emergence and growing interest in tiltrotor air vehicles sparked a renewed focus on the phenomenon of VRS. Scientists and engineers investigated whether existing experimental correlations, computed for conventional helicopters, would extend to tiltrotor configurations, following a series of incidents involving tiltrotor platforms. Notably, a high-profile accident involving the Bell-Boeing V-22 Osprey was attributed, at least in part, to the onset of VRS during a critical phase of flight.

For instance, Betzina [10] focused specifically on the Bell-Boeing V-22 Osprey by experimentally investigating the VRS phenomenon on a scaled version of the rotor-wing configuration and found that, in ad-

dition to the expected reduction in thrust, VRS could cause severe low-frequency roll oscillations coupled with thrust fluctuation with the same frequency content.

Notable work was done by Johnson [11], which extensively surveyed the existing literature to develop a VRS model which would extend across different aerial platforms and provide a low-order model for predictions and real-time simulations. The developed model proved successful in predicting the tilt-off behaviour of tiltrotor configurations, despite the significant difference in the insurgence VRS in conventional helicopters.

On the topic of VRS models, Basset et al. [12] utilised numerical simulations to evaluate various criteria for predicting VRS boundaries, obtaining consistent results with flight test data.

Throughout the last decade, research on a new kind of aerial platform intensified: electric vertical take-off and landing (eVTOL) vehicles have been investigated, to optimise the design and deployment of air vehicles in the scope of electric urban air mobility (UAM) and public services such as early wildfire fighting, humanitarian crisis and last-mile delivery, Doo et al. [13]. Multiple lines of research have been developed, spanning from preliminary aircraft design [14] and passenger acceptance [15], to vertiport design and integration in urban environments [16].

Concerns arose in the scientific community regarding the behaviour of such novel air vehicle designs in VRS: Brown [17] found that eVTOL platforms exhibit VRS at higher forward flight speeds compared to conventional helicopters, due to the higher disc loading and resulting higher induced velocity. Additionally, eVTOLs are often designed to operate in urban environments, where aggressive descent manoeuvres may represent a critical flight condition.

Veismann et al. [1,18] performed an experimental investigation of small-scale multicopter rotors in axial descent, focusing on the interactional effects of rotors in a side-by-side configuration at multiple separation distances and for various geometrical parameters. Interestingly, it was found that, in VRS, a singular vortex ring structure formed around the dual rotor configuration at small rotor separation distances. However, the dual rotor configuration showed very similar performance to the reference single rotor configuration. It is worth noting, however, that the experimental investigation assessed only the axial descent condition, without taking into consideration different descent angles.

Likewise, Chae et al. [19] performed an experimental campaign focusing on small-scale multicopter rotors in axial descent. In this case, however, the authors fixed the rotor's geometry and focused on the rotor separation distance only, by performing loads and velocimetry measurements. Interestingly, following the work of Green et al. [20], the authors were able to quantify the occurrence of the toroidal flow topology in the VRS onset regime and found that reduced rotor separation distances made the configuration less prone to fall into the VRS regime. However, as the rotors fell into fully-developed VRS, the probability of falling into VRS did not change for the dual rotor configuration, as it persisted in the tubular flow topology independently from rotor separation distance. Nonetheless, the flow field in fully-developed VRS was still affected by the rotor interactional effects, indicated by the disruption of the vortex ring in the inner region between the rotors. Indeed, for low rotor separation distances, the flow field developed a single recirculating region, engulfing both rotors in the configuration.

Savino et al. [21], on the other hand, tested a single rotor which equips the Archer Aviation's Maker eVTOL, by combining loads and velocimetry measurements, again in axial descent only. Although the work focuses on the single rotor configuration, hence neglecting the rotor-rotor interactional effects, it provides experimental data on propeller-like rotors, which have been very rarely investigated in VRS studies. In fact, the rotors used in eVTOL configurations are often optimised for forward flight, leveraging highly twisted and tapered blades. Indeed, blade geometry was proved to play a crucial role in defining the rotor's behaviour in VRS, as in Brown et al. [22].

In the scope of the "GARTEUR AG28: Vortex Ring State", Bucherelli et al. [23] performed loads, power and velocimetry measurements on dual rotors in side-by-side configuration in axial descent. Particularly, the authors focused on systematically evaluating the effect of rotor separation distance and sense of rotation, with the single isolated rotor used as a reference case. The primary configurational effect found for the dual rotor configuration is a premature occurrence of the VRS phenomenon, which is shifted towards the hover condition. In addition, depending on the rotor separation distance, the severity of thrust reduction is modified as well: as the rotor separation distance is reduced from 1 radius to 0.1 radius, thrust in VRS progressively decreases, going from a 10% to a 15% reduction over the hover case, matching the thrust reduction values found for the isolated rotor. In other words, as the rotor separation is reduced, the configuration starts to behave more like the isolated single rotor configuration, at least in terms of thrust reduction.

The current work aims to experimentally investigate the VRS for multiple descent angles, for 1-rotor, 2-rotor and 4-rotor multicopters using thrust and power measurements, as well as planar stereoscopic particle image velocimetry (S-PIV).

The remainder of the manuscript is organised as follows. Section 2 describes the experimental setup, including the rotor rig (Section 2.1) and the S-PIV system (Section 2.2). Section 3 presents the data-reduction procedure, including the adopted normalisation and the definition of the relevant variables. The experimental results are presented and discussed in Section 4, with aerodynamic-load measurements addressed in Section 4.1 and velocimetry results in Section 4.2. The main conclusions are summarised in Section 5. Finally, Appendix A provides additional considerations on alternative normalisation approaches for the load data.

2. Experimental setup

The experiments were conducted in the Rotor Test Facility Göttingen (RTG) of the German Aerospace Centre (DLR). A photograph of the experimental setup taken during the S-PIV campaign is shown in Fig. 2. In the scope of the current VRS experiments, the RTG provides a recirculating wind tunnel with an open test section (cross-section 1.6 m × 1.6 m) used to simulate the descent velocity component. To simulate this flight condition, the rotor axes have been oriented horizontally, with their downwash facing the incoming jet of the wind tunnel. The support structure hosting the motors is placed on a tiltable platform, which allows for accurate control of the relative angle, α, between the rotor plane and the freestream velocity, U_∞. Indeed, by changing α and U_∞, one can simulate different descent angles and vertical velocities. A sketch of the simulated flight condition is displayed in Fig. 3, where different views of the quadrotor configuration are presented. The red, blue and black arrows represent the descent and horizontal velocity vectors, V_v and V_h, respectively, and their sum U_∞. Additionally, an axonometric view of the four rotors is also reported for illustrative purposes, showing the quadrotor configuration in descent flight.

2.1. Rotor rig

The quadrotor setup was similar to that used in [24–26], but using slightly larger propellers, since those were discontinued by the manufacturer. The experiment uses a 2-bladed, fixed-pitch multicopter rotor of type KDE 15.5x4.3" with a 0.196 m radius. Chord, thickness and twist distributions are shown in Fig. 4 along with some representative airfoil sections fitted on the blade. Up to four 180 W brushless DC motors with a rotation rate of 4800 RPM (80 Hz) were used for all test cases, resulting in a diameter Reynolds number of $Re_D = 2.6 \times 10^6$. In hover, the rotor generates about $T_{hov.} = 13.5$ N of thrust, leading to a disc loading of $DL = 113\,\mathrm{N/m^2}$. Four different configurations have been tested: the Single Rotor (SR), which will be used as a reference configuration, the Dual Rotors arranged in a Side-by-Side configuration (DRSbS), the Dual Rotors in Tandem configuration (DRT) and the Quadrotor configuration

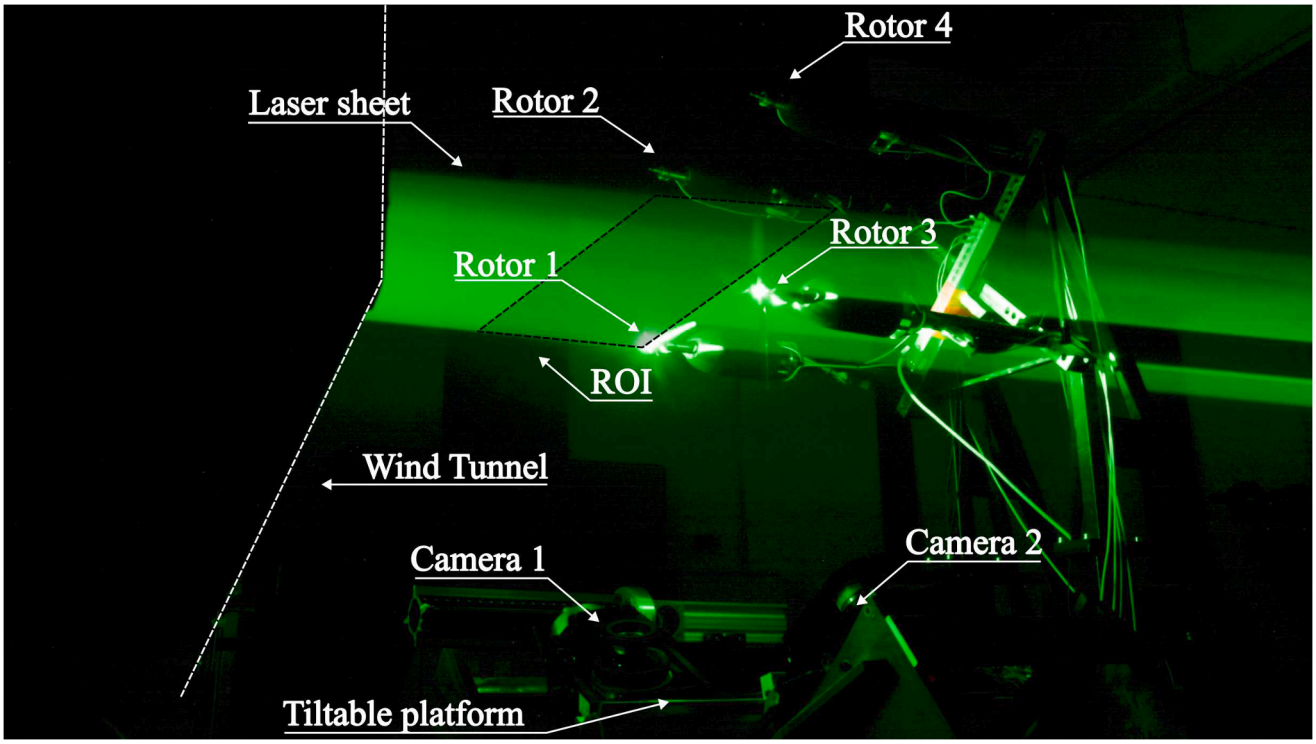


Fig. 2. A photograph of the experimental setup during S-PIV recordings.

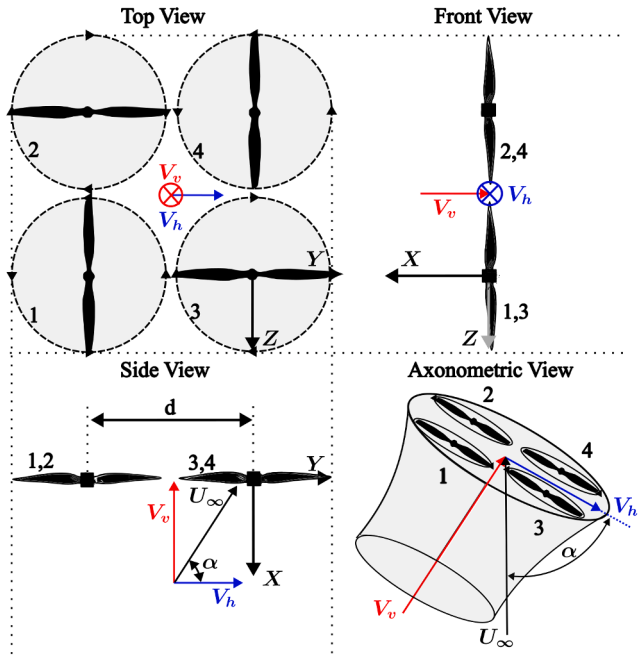
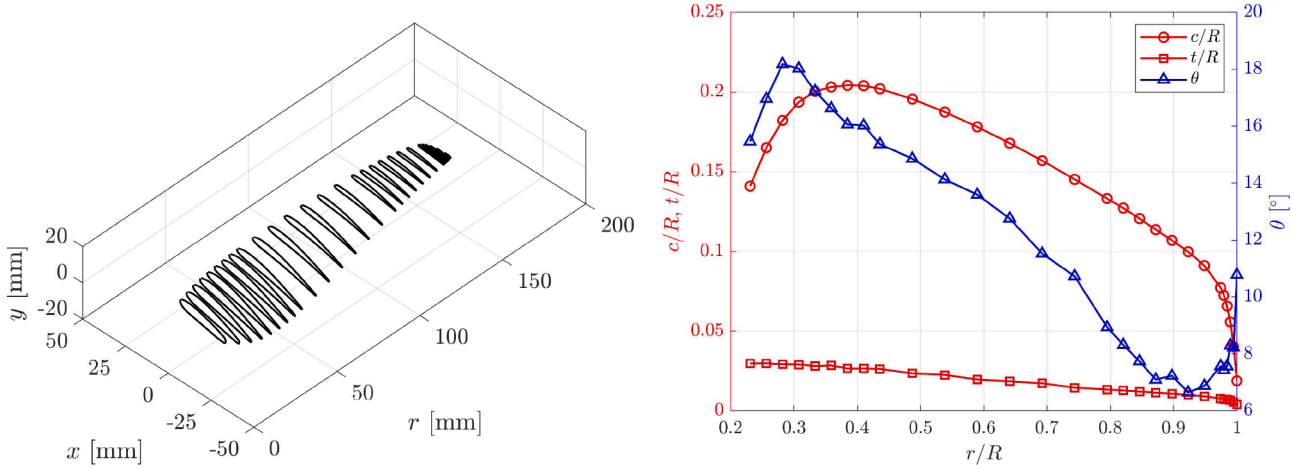


Fig. 3. Schematic representation of the quadrotor configuration in multiple views.

(QR). The QR configuration is obtained by operating all four motors simultaneously, whereas the DRSbS and DRT configurations combine rotor 1 and 2 and rotor 1 and 3, respectively, Fig. 3. All multirotor configurations are set to operate in the tip-to-gap configuration, *i.e.* with a constant phase shift of 90° between neighbouring rotors, and with a rotor separation distance of $d = 1.05D$, as shown in Fig. 3. During the experiments, the rotor phase and rotation rate were monitored, remaining within 1° of the expected position at all times. Additional relevant flow parameters, such as wind tunnel exit velocity, ambient air pressure, temperature, and density, have been simultaneously acquired via a multi-channel data logger from Dewetron.

2.2. S-PIV setup

A stereoscopic particle image velocimetry setup has been developed to investigate the flow field around the device for multiple descent angles, descent velocities and configurations The S-PIV setup features two 2560 × 1600 pixels Phantom VEO 640L CMOS cameras for image pairs acquisition, positioned with the opening angle between the camera axes set at 100 °. The cameras were positioned on the rotating platform to maintain the same field of view (FOV) irrespective of the tested descent angle. The cameras are equipped with two 24 mm f#2.5 lenses, motorised Scheimpflug adapters and are positioned at approximately 500 mm from the laser sheet plane, yielding a magnification factor of ≃3.5 pixel/mm. The cameras are operated at 15 Hz, and the proprietary software from LaVision, DaVis 11, is used for image acquisition. Stroboscopic illumination is provided by a double-pulsed Nd:YAG laser by Evergreen, capable of outputting 200 mJ at 15 Hz. The laser beam is shaped into a laser sheet about 5 mm thick. The laser sheet is shaped outside the wind tunnel, where the laser sheet optics are placed, and then it is projected in the measurement region by means of two 45° mirrors. The last mirror is placed inside the wind tunnel and is fixed in place using a micrometric rail for fine adjustments. The flow is seeded using DEHS fed into a CTS 1000 particle generator by Seika, producing particles with an average size of about 2 μm in size. The deployment of the experimental setup is as follows: the laser sheet is aligned with rotors 1 and 3, which are the bottom rotors of Fig. 2, passing through both rotors' hubs. The adopted reference system is shown in Fig. 3 and it is centred on the hub of rotor 3, with X indicating the streamwise direction, Y the crosswise direction and Z the out-of-plane direction. Flow fields will be presented as in the side view shown in Fig. 3. Stereoscopic calibration has been carried out using the LaVision Type 31 two-plane calibration target and the Pinhole camera model, yielding a stereo calibration error smaller than 0.1 pixel. A total of 700 images were acquired for each



(a) 3D representation of the airfoils fitted on the rotor blade.

(b) Chord, c, thickness, t, and twist, θ, radial distributions.

Fig. 4. A summary of the geometrical characteristics of the KDE 15.5x4.3" blade.

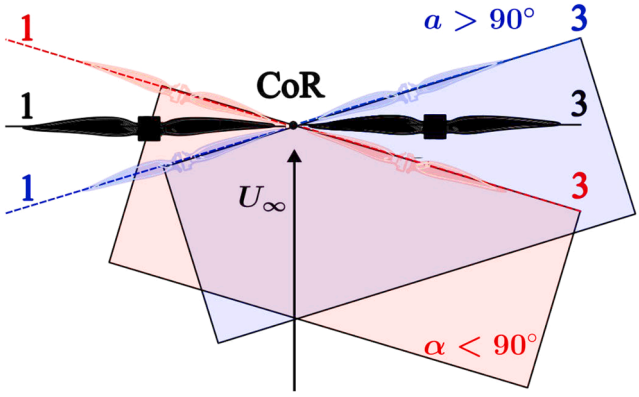


Fig. 5. Alternative ways of measuring the flow field around the quadrotor at $\alpha < -90°$ (—) and at $\alpha > -90°$ (—). (For interpretation of the references to colour in this figure legend, the reader is referred to the web version of this article.)

time average S-PIV flow field. The region of interest (ROI) roughly measures $2.6\,R \times 4.3\,R$, where R is the rotor radius, in the streamwise and crosswise directions, respectively. This ROI proves adequate for the SR configuration, where only one rotor is visible in the FOV. For the QR configuration, however, the device extends for over four radii in the Y direction, making the current FOV too narrow to capture the flow structures extending past the front and back rotors. Hence, the following procedure has been developed to achieve an extended ROI (eROI), while still maintaining the same resolution and optical setup. Referring to Fig. 5, the image displays a schematic representation of the alternative ways of achieving a given α. Leveraging the symmetry of the device with respect to the wind tunnel exit section, the same descent angle can be achieved by rotating the tiltable platform either in clockwise or counter-clockwise directions along the Z axis, given the positioning of the centre of rotation (CoR) in the middle of rotor 1 and rotor 3. However, the optical setup does not have the same symmetrical properties as the FOV includes only half of rotor 1 and the entirety of rotor 3. In other words, rotors 1 and 2 become the front rotors for $\alpha < 90°$, while, on the contrary, rotors 3 and 4 become the front rotors for $\alpha > 90°$. Thus, by capturing the same descent angle both in the clockwise and counter-clockwise directions of rotation, the two FOVs can be stitched to obtain the mentioned eROI, which extends to $2.6\,R \times 5.8\,R$ in the streamwise and crosswise directions, respectively.

3. Data reduction

A preliminary experimental campaign has been conducted, focusing on the acquisition of the aerodynamic data for each of the tested configurations. Care needs to be taken with the non-dimensionalisation of the data, since the experiments were performed with a constant rotation rate of the rotor, rather than trimming to constant thrust. The data has been non-dimensionalised with the induced velocity, $V_{ref.}$, computed from the measured thrust for every configuration, as in (1):

$$V_{ref.} = \sqrt{T/2\rho A} \tag{1}$$

where A is the rotor disc area, T the measured thrust averaged over the entire sample and ρ the measured air density. Alternatively, a different choice for the reference velocity can be made: $V_{hov.} = \sqrt{T_{hov.}/2\rho A}$. More details on the choice of the reference velocity are provided in Appendix A. Horizontal, V_h, and vertical, V_v, velocities are computed using the following decomposition, (2) and (3):

$$V_v = U_\infty \sin(\alpha) \tag{2}$$

$$V_h = U_\infty \cos(\alpha) \tag{3}$$

where U_∞ is the wind tunnel speed and α is the descent angle. An Eulerian reference frame will be considered for the remainder of the document, with the device stationary in space and the incoming dynamic pressure generated by the wind tunnel, as in the experimental setup. Following the work of Johnson [11], the characteristic curves will be presented in terms of the induced velocity by the rotor, V_i, and in terms of the overall velocity through the rotor, $V_v + V_i$, which is a measure of the rotor's required power. Both will be non-dimensionalised with the reference velocity, $V_{ref.}$, which has already been introduced in Eq. (1) as a scaling factor. Even though momentum theory is not applicable for the VRS regime, as explained in the introduction of this document, the following Eqs. (4) and (5) can be used to derive the mentioned characteristic curves in VRS, where momentum theory is invalid. The electrical required power is measured, and is related to the total required mechanical power, P, by a dynamometer calibration of the motor and control system.

$$\frac{V_i}{V_{ref.}} = \frac{P - P_0}{T V_{ref.}} - \frac{V_v}{V_{ref.}} \tag{4}$$

$$\frac{V_v + V_i}{V_{ref.}} = \frac{P - P_0}{P_{ref.}} \tag{5}$$

Where P and T are measured, with $P_{ref.} = T V_{ref.}$ being the reference mechanical power measured. On the other hand, P_0 is the required power stemming from profile drag and is estimated using the following

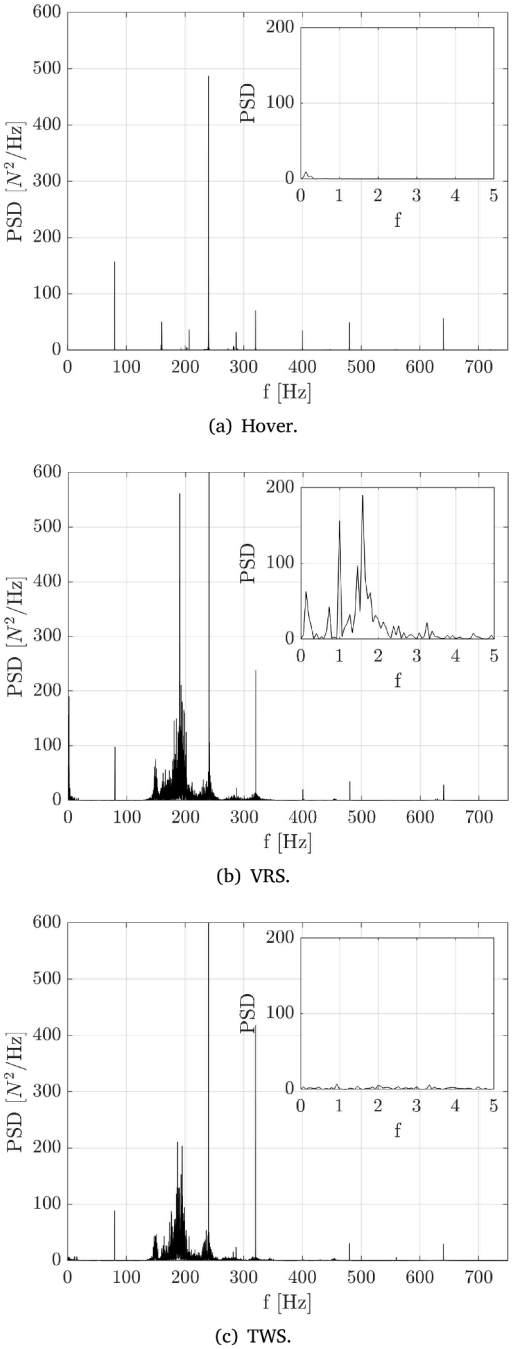
relation: $P_0 = \frac{\sqrt{2}}{8}\rho C_d \sigma \Omega^3 \pi (D/2)^5$, where Ω, σ and D represent the rotor's angular velocity, solidity and diameter, respectively. C_d is the sectional drag coefficient, which is set to $C_d = 0.0170$ for all configurations[1] Using Eqs. (4) and (5), one can derive the characteristic curves for a given configuration based on performance measurements only, with additional modelling only required to give an estimate of the profile power. For the scope of this work, the approach proposed by Johnson [11] was followed: profile power has been assumed to be independent from V_v and V_h and the configuration.

4. Results and discussion

4.1. Loads

A preliminary thrust measurement campaign has been conducted using the strain gauge balances integrated into the motor unit to explore different combinations of descent angles and incoming flow velocities. Additionally, the motor power was measured. Loads and power data has been acquired at 30 kHz. A spectral analysis of the thrust signals has been carried out for different flight conditions to deduce a cut-off frequency to low-pass philtre the acquired data and derive a characteristic frequency of the phenomenon. The images shown in Fig. 6 display the power spectral density (PSD) of the thrust signal plotted against frequency for the SR configuration at $\alpha = 70°$. In addition, every diagram features a subplot positioned in the top-right corner that shows an enlargement of the same PSD distribution for the frequency range of $f \in [0; 5]$ Hz. Three flight conditions are comparatively assessed: hover, VRS and turbulent wake state (TWS). TWS is reached when the descent velocity is increased from VRS, and the mean flow direction through the rotor disc is directed upwards, $V_v + V_i < 0$. Recirculation regions still form, but they are placed above the rotor, see Fig 1c. Starting with the hover condition, presented in Fig. 6a, the PSD distribution shows isolated power peaks for values corresponding to integer multiples of the 1/rev frequency in the 80 to 640 Hz range. Such behaviour is expected due to the rigid mounting of the rotor blades and hub to the support structure. Very similar results are reported in Betzina [10]. Moving on to Fig. 6b, the effect of the VRS regime is introduced. To accentuate the effect of the VRS, the displayed PSD distribution refers to the most severe thrust reduction measured for $\alpha = 70°$, which equals to $T/T_{hov.} \simeq 0.8$, where $T_{hov.}$ represents the thrust generated in hover. The PSD distribution shows the same power peaks corresponding to the integer multiples of the 1/rev frequency, as shown in 6a. However, two additional broader-banded contributions to the power spectrum are visible in the 150-300 Hz and 0-5 Hz ranges.

Finally, Fig. 6c shows the PSD distribution for the TWS regime. Similarly to the VRS condition, the displayed measurement point has been selected as the one that maximises the thrust variation in TWS regime, which equals to $T/T_{hov.} \simeq 1.3$. Comparing Fig. 6b and c, the PSD distributions show similar behaviours in the 150 to 300 Hz range, which are caused by the wind tunnel contribution. However, by comparing the enlargements in the top right corner, the PSD in the TWS regime lacks the power contributions in the 0 to 5 Hz range. The comparative assessment of the PSD distributions across different regimes proved that the frequency range characteristic of the VRS regime is located between 0 and 30 Hz, and, for this reason, thrust time series have been low-pass filtered at 30 Hz via a sliding average philtre. In addition, the spectral analysis revealed a clear frequency associated with an increased power content in the VRS regime at $\omega \simeq 1.6$ Hz, which is the highest power peak visible in Fig. 6b, enlargement in the top right corner. Following the work of Johnson [11], the frequency scaling in VRS is defined as follows: $\omega_{\text{VRS}} = V_{hov.}/R$. In the current work $\omega_{\text{VRS}} \simeq 35$ Hz, which leads to the



(a) Hover.

(b) VRS.

(c) TWS.

Fig. 6. PSD of the thrust signal for different flight conditions: hover (a), VRS (b) and TWS (c), for the SR configuration at a descent angle of $\alpha = 70°$.

definition of the following non-dimensional frequency: $\omega/\omega_{\text{VRS}} \simeq 0.05$, which, again, is consistent with the data obtained by Betzina [10].

Fig. 7 reports on the normalised thrust time series signals for three different flight conditions, VRS, hover, and TWS at $\alpha = 70°$. The plotted normalised thrust is defined as follows: $T_{inst.} - T/T_{max}$, where $T_{inst.}$ is the low-pass filtered thrust signal and T_{max} is the maximum thrust measured in the sample. Fig. 7 is presented to highlight the oscillatory nature of the thrust signal in different flight conditions. Each curve displays the low-pass filtered signal at 30 Hz. Comparing the thrust signal measured in VRS with the thrust signal in hover and TWS conditions, a significant reduction in fluctuations can be observed. Moreover, for the thrust signal measured in VRS, fluctuations show a low-frequency periodicity, which is lacking in hover and in the TWS regime. Such low-frequency

[1] The sectional drag coefficient has been computed via blade element momentum theory for a representative section at 75% of the radius.

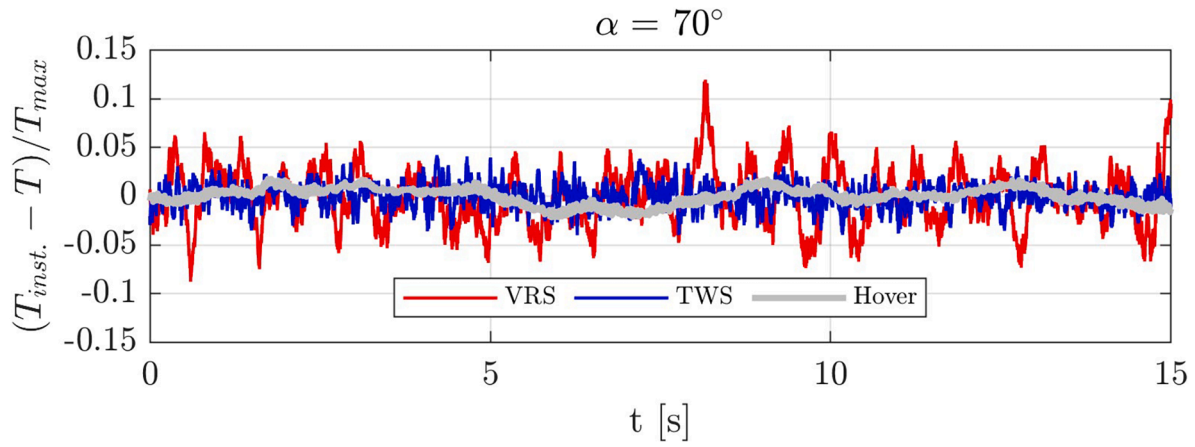


Fig. 7. Low-pass filtered normalised thrust time histories for the SR configuration at $\alpha = 70°$ in different flight conditions, VRS (—), hover (—), and TWS (—). (For interpretation of the references to colour in this figure legend, the reader is referred to the web version of this article.)

periodicity has been associated with the accumulation and shedding of vorticity in the recirculating wake of the rotor in VRS, as in Newman et al. [27,28]. Even though the flow in TWS still manifests relevant unsteady behaviour, the rotor wake does not experience the mentioned periodical build-up and shedding of vorticity underneath the rotor, which causes the low-frequency content in the thrust signal in VRS. The severity of such thrust fluctuations has been quantified using the root mean square (RMS) of the normalised low-pass filtered thrust signal deprived of its mean, as in Fig. 8 where the RMS($\Delta T/T$) is presented for all measured combinations of descent velocities, descent angles and configurations, where $\Delta T = T_{inst.} - T$.

Starting with the SR configuration, it is worth noting that the trends shown for $\alpha = 70°$ in Fig. 7 extend to the entire span of tested descent angles. For every α, the RMS gradually grows as the descent velocity is reduced and then starts to decrease as the rotor exits the VRS condition, approaching the TWS state. The maximum RMS is reached for $V_v/V_{ref.} \simeq -1.25$ at $\alpha = 90°$ and is equal to RMS($\Delta T/T$) = 0.15. As the descent angle is reduced, the RMS of the thrust signal also progressively decreases. Together with the mean reduction in RMS, the descent velocity which corresponds to the highest RMS, is progressively increased as the descent angle gets smaller. Such a reduction in RMS found for smaller descent angles can be explained again by recalling the work of Newman et al. [28]: in the dynamic balance of vorticity deposited by the rotor into the wake and vorticity transported away, the forward velocity plays a key role in preventing the rotor from falling into VRS. In this sense, moving from larger to smaller α in Fig 8, causes the horizontal velocity to increase, preventing the configuration from falling into VRS. These considerations, made for SR, hold for the other configurations. Nonetheless, some configuration-specific effects take place, which can be addressed by comparing the different panels of Fig. 8.

Comparing the SR and DRSbS configurations, the RMS distributions exhibit very similar distributions, both in terms of absolute values as well as of overall shape, with the thrust fluctuations growing progressively, reaching a plateau and then reducing for decreasing descent velocities, leading to a maximum in thrust fluctuations of RMS($\Delta T/T$) = 0.15. Moving on to the DRT configuration, the RMS distributions change significantly compared to SR and DRSbS: thrust fluctuations grow in a quasi-linear fashion, reaching a maximum of RMS($\Delta T/T$) = 0.225 for $V_v/V_{ref.} \simeq -1.20$ at $\alpha = 90°$. From this point, further reducing the descent velocity causes the thrust fluctuations to drop rapidly, again quasi-linearly, although at a faster rate. Moving to the QR configuration introduces similar modifications to the RMS distribution, although significantly exacerbated compared to the DRT configuration: the maximum RMS is even higher, reaching RMS($\Delta T/T$) = 0.3 for $V_v/V_{ref.} \simeq -0.9$ at $\alpha = 90°$. Again, the plateau found for the SR and DRSbS configurations disappears, and the thrust fluctuations grow and decay linearly, although at a faster rate compared to the DRT configuration. It should be borne in mind that the RMS distributions shown herein are computed using the low-pass filtered time histories; hence, the larger thrust fluctuations observed in the multirotor cases cannot be ascribed to high-frequency structural vibrations arising from the rigid mounting of the motors on the supporting platform. Additionally, the RMS distributions for the QR configuration also show a rather anticipated peak in fluctuations compared to the other test cases. This represents an undesirable behaviour of the configuration, as it poses a greater risk of experiencing intense thrust-induced vibrations, especially for large angles of descent. Finally, as indicated in Johnson [11], a good measure for the thrust-induced vibrations is given by multiplying the measured RMS by a factor of 3. As a consequence, the difference in vibrations experienced by the QR configuration compared to the other test cases is even greater.

Data acquired during the aerodynamic load campaign have been condensed into a single scatter plot which combines information about the flight condition, namely V_v, V_h and α, and the relative value of thrust reduction/increase over the hover case. Such a graph will be referred to as a flight path plane (FPP), since it describes the mean thrust variation for different combinations of horizontal and descent velocities. The adoption of this kind of graph is customary [8,10–12,17,22,29,30] for the analysis of the VRS regime since it provides an overview of the most critical flight paths in descending flight. Fig. 9 shows the FPP scatter plots for all four different configurations. Every circle marker identifies a single data entry in the test matrix of the aerodynamic load campaign, and it is associated with the mean thrust value computed over a 30-s acquisition window. For the multirotor configurations, thrust values are also averaged across the rotors. The mentioned circle markers are colour-coded, with red, white and blue indicating reduction, no variation or increase in thrust over the hover case, respectively. The solid and dashed black lines connecting the dots are obtained via Delaunay triangulations and respectively represent a mean thrust reduction threshold of 5% and 15%. The mentioned Delaunay triangulations can provide a quantification of the VRS boundaries: the innermost region, identified with the solid black line, defines the so-called *deep* VRS region where thrust is severely reduced, and control authority over the air vehicle is compromised. Indeed, the most crucial boundary is the outermost, identified with the dashed line and termed *shallow* VRS. In this region, only a modest reduction in thrust is observed, while attitude control can already be impaired. Furthermore, the VRS boundary computed using the model developed in Johnson [11] is displayed with grey square markers. Starting with Fig. 9a, the *deep* VRS region is confined roughly to $V_v/V_{ref.} \in [-1.5; -1.1]$ and to $V_h/V_{ref.} \in [0; 0.5]$, whereas the *shallow* VRS region extends further, reaching vertical velocities as high

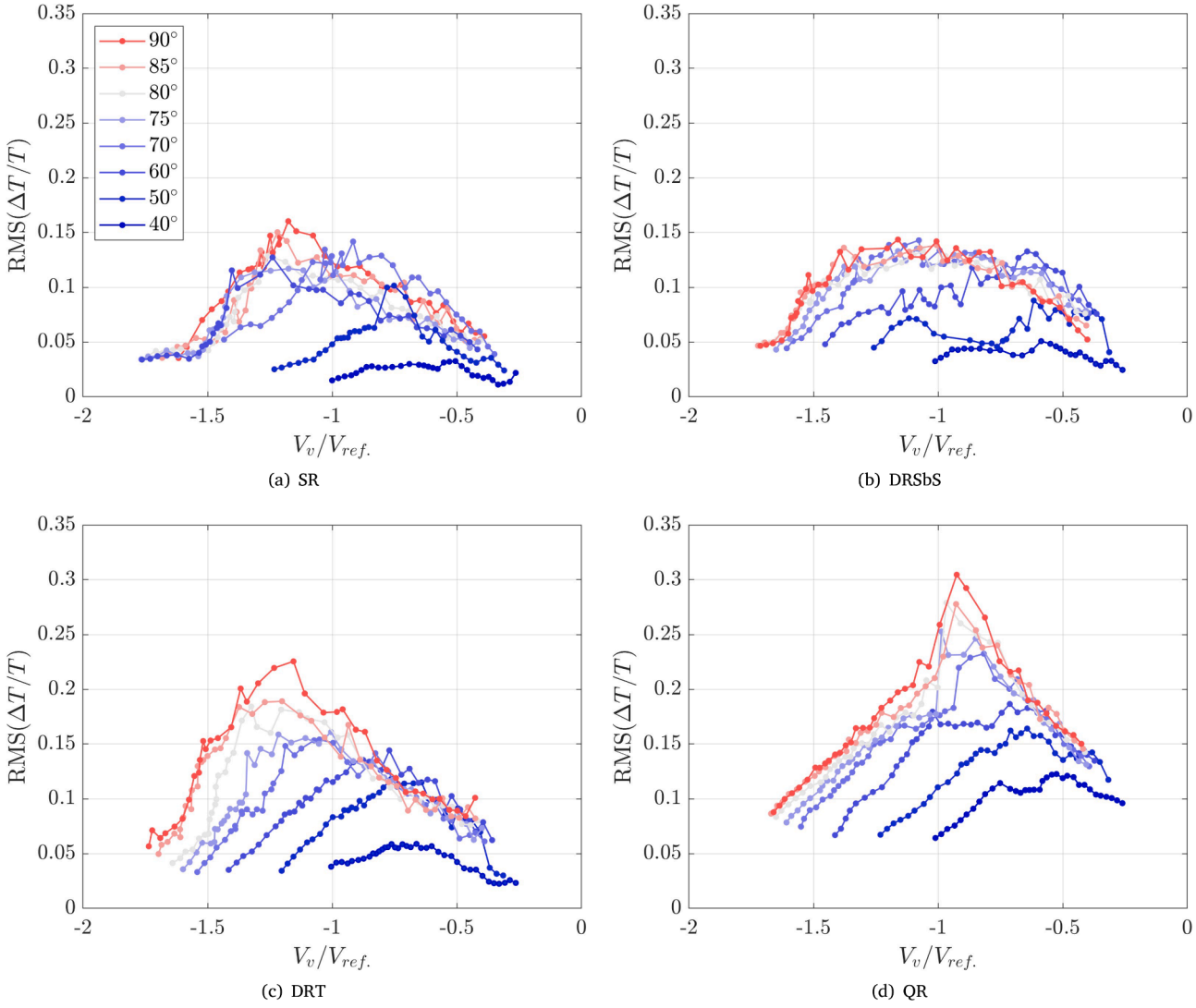


Fig. 8. Non-dimensional thrust RMS computed for individual rotors in the configuration, plotted against descent velocities for different descent angles, (a) SR, (b) DRSbS, (c) DRT and (d) QR configurations.

as $V_v/V_{ref.} = -0.8$, while extending to significantly higher horizontal velocities of up to $V_h/V_{ref.} = 0.8$. A progressive entrance and a rather sudden exit from the VRS regime can be observed for the SR configuration: starting from the hover condition and increasing the descent velocity, the *shallow* and *deep* VRS boundaries are significantly further apart when entering than when exiting VRS, with the two boundaries almost overlapping at $V_v/V_{ref.} = -1.5$. Although the overall characteristics of the FPP scatter plot described for SR are preserved for the other configurations as well, moving to the multirotor configurations causes the VRS onset to shift to a higher descent velocity. For reference, the SR configuration enters the shallow VRS region for $V_v/V_{ref.} = -0.8$, regardless of the descent angle. The DRSbS configuration, conversely, enters the same VRS region for descent velocities as high as $V_v/V_{ref.} = -0.55$. Similarly, the DRT configuration exhibits an anticipated VRS onset compared to SR, although with a strong dependency on α: for $\alpha \in [80°; 90°]$ the DRT configuration behaves analogous to the baseline configuration, entering the shallow VRS region for $V_v/V_{ref.} = -0.8$; however, as α is reduced, the VRS onset is progressively shifted towards higher descent velocity values, moving up to $V_v/V_{ref.} = -0.5$ for $\alpha = 50°$. A similar modification in the extent of the shallow VRS region can be observed for the QR configuration, featuring a similar dependency on α. One could argue that this shift towards higher descent velocities is even more pronounced for QR, as the upper boundary moves to approximately $V_v/V_{ref.} = -0.55$, even for $\alpha \in [80°; 90°]$. The similarities between the DRT and QR configurations can be ascribed to the rotors' layout, which in both test cases is set to a front/back arrangement. For $\alpha < 90°$, this causes the rotors in the rear to operate in the wake of the ones at the front, degrading their aerodynamic performance and delaying the exit from VRS. Additionally, the QR configuration also exhibits a significant shift of the *deep* VRS region towards higher descent velocities, as it extends across the following velocity ranges: $V_v/V_{ref.} \in [-1.3; -0.8]$ and $V_h/V_{ref.} \in [0; 0.4]$. Despite the different extent of the VRS regions for the various configurations, the maximum thrust reduction is similar for all configurations.

In general, the configurational effects that have been quantified via Fig. 9 are mostly detrimental, as they cause the VRS regions to move to higher descent velocity, potentially closer to useful zones of the flight envelope. Particularly, for the DRT and QR configurations, the specific arrangement of the rotors renders the beneficial effects of the forward velocity component less efficient in preventing VRS to occur/persist, which extends to combinations of higher descent and forward velocity.

It is critical to point out that the modifications in the FFP plot that have been discussed herein should be complemented with additional considerations regarding the modification of the FPP, but expressed in its dimensional form, *i.e.* using the dimensional vertical and horizontal

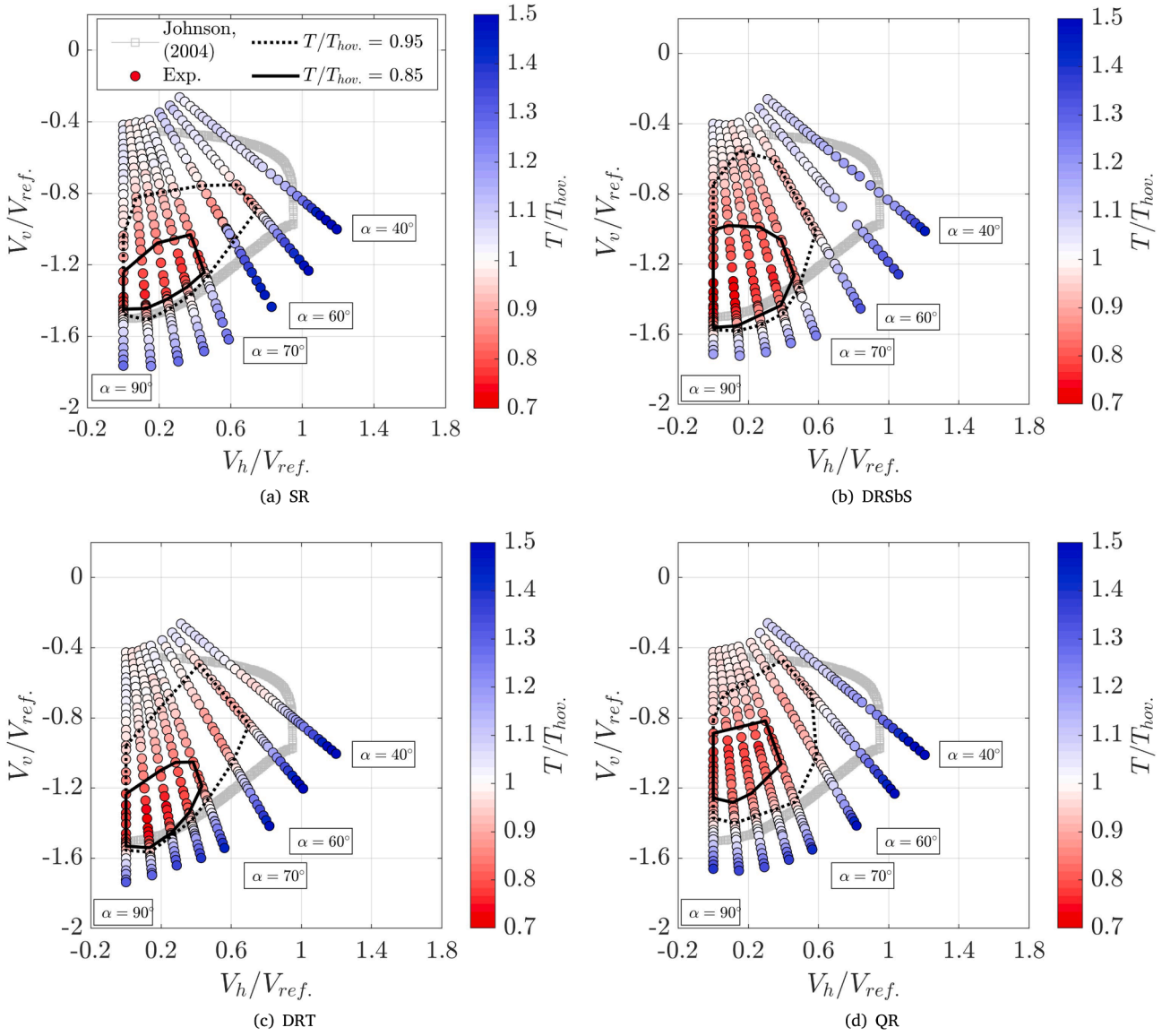


Fig. 9. Flight path plane scatter plots coloured with mean thrust value modifications over the hover case for the (a) SR, (b) DRSbS, (c) DRT and (d) QR configurations. Red (•), white (∘) and blue (•) indicate a reduction, no variation and an increase in thrust over the hover case, respectively. Black lines indicate Delaunay triangulation for a thrust reduction threshold of 0.95 and 0.85, indicated by a solid (—) and dashed line (·····), respectively. Grey markers (■) indicate the VRS boundary computed by Johnson [11].

velocity. By doing so, the FPP plot would then provide information on the effect of disc loading, which is not considered in Fig. 9. As initially noted by Stewart [31], the size of the VRS region scales with the square root of the disc loading when plotted in dimensional terms. This relation was then thoroughly analysed more recently by Brown [17] in the scope of VRS for eVTOL platforms, as this rather new concept of air vehicle promises unprecedented combinations of reduced weight and large disc loading. Indeed, the information presented in Fig. 9 should be interpreted as configuration-related effects only that do not account for disc loading, which would then need to be *added*, provided that the considerations on the scaling of the VRS region hold for the data presented herein. The choice of presenting the FFP plot in its non-dimensional form is made firstly to isolate the configurational effects and, secondly, because the relation between the number of rotors and disc loading is not trivial, as it depends on the specific design of the aerial platform.

Fig. 10 presents the same FPP scatter plots for all combinations of horizontal and descent velocities and for each configuration as in Fig. 9, with the markers now colour-coded according to the RMS of the normalised thrust fluctuations, RMS($\Delta T/T$). Although RMS($\Delta T/T$) has already been discussed in detail in relation to Fig. 8, its representation on the FPP in Fig. 10 enables a direct comparison between the regions of the flight envelope characterised by the highest thrust reduction and those associated with the largest thrust fluctuations. Comparing Figs. 9 and 10, a strong configurational effect can be observed, with the QR configuration exhibiting larger thrust fluctuations than the SR test case across the entire flight envelope. A further configurational effect emerges from the comparison between Fig. 10b and c: when the rotors are arranged in a tandem configuration, they experience larger thrust fluctuations than in the side-by-side arrangement. In general, regions of high thrust fluctuations appear to correlate well with the regions of the flight envelope characterised by the greatest thrust reduction. In particular, for the QR configuration, the upper boundary of the *deep* VRS region shown in Fig. 9d, identified by $T/T_{hov.} < 0.85$, appears to correspond to the largest thrust fluctuations measured, as shown in Fig. 10d. Beyond this boundary, approximately located at $V_v/V_{ref.} \simeq -0.9$, the thrust

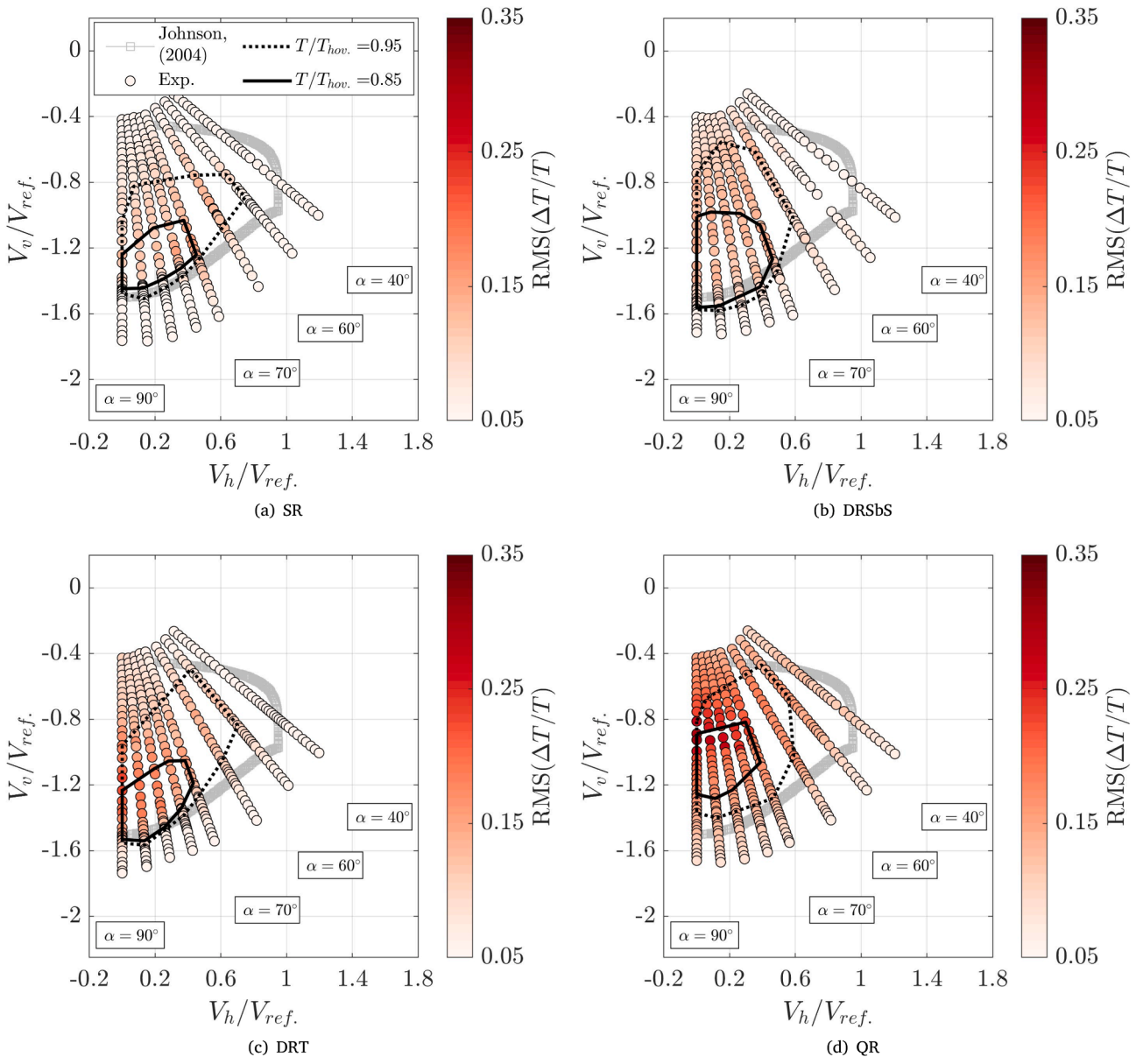


Fig. 10. Flight path plane scatter plots coloured with non-dimensional thrust RMS for the (a) SR, (b) DRSbS, (c) DRT and (d) QR configurations. Black lines indicate Delaunay triangulation for a thrust reduction threshold of 0.95 and 0.85, indicated by a solid (—) and dashed line (·····), respectively. Grey markers (■) indicate the VRS boundary computed by Johnson [11].

fluctuations tend to decrease as the descent velocity is increased, whereas the thrust reduction remains severe, with $T/T_{hov.} < 0.85$.

Fig. 11 displays non-dimensional thrust values for all four configurations and for all descent angle/descent velocity combinations.

Starting with SR, the reduction in thrust caused by entering the VRS condition is quasi-linear up to a certain descent velocity, after which thrust starts to be restored. Again, thrust increases almost linearly, although at a much faster rate. Depending on the descent angle, the minimum thrust varies significantly, increasing for decreasing descent angles, together with the reference descent velocity at which such a minimum is observed. For SR at $\alpha = 90°$, the minimum thrust is measured at $V_v/V_{ref.} \simeq -1.42$ and equals $T/T_{hov.} \simeq 0.72$.

The DRSbS configuration exhibits a similar behaviour to SR in terms of $T/T_{hov.}$ shape distribution, although reaching a lower minimum thrust value of $T/T_{hov.} = 0.70$ for $V_v/V_{ref.} \simeq -1.36$.

The DRT and QR configurations, however, display a more peculiar behaviour when entering VRS: the reduction in thrust is non-linear, as the $T/T_{hov.} \simeq 1$ up until $V_v/V_{ref.} \simeq -0.75$, only to decrease rapidly afterwards. For the DRT, however, as α is reduced, this behaviour progressively fades, while, for QR, it persists to shallower descent angles. Additionally, while the DRT configuration still exhibits a minimum thrust level equal to $T/T_{hov.} \simeq 0.74$ at $V_v/V_{ref.} \simeq -1.42$, the QR configuration experiences its minimum thrust of $T/T_{hov.} \simeq 0.78$ at about $V_v/V_{ref.} \simeq -0.99$. Furthermore, the QR configuration exhibits a significantly different behaviour while exiting VRS, as thrust is more slowly restored with decreasing $V_v/V_{ref.}$.

The data presented in Fig. 11 can be further analysed by plotting the thrust levels of different rotors in the configuration: as a result, Fig. 12 reports on the thrust reduction levels experienced by individual rotors for all four configurations and descent velocity at three selected descent angles: $\alpha \in [40°, 60°, 90°]$. Recalling that rotors 1 and 2 are the front rotors, while rotors 3 and 4 are the rear ones, the comparative assessment of the subplots of Fig. 12 highlights that, as the descent angle is reduced, the rear rotors output less thrust than the ones at the front. For Figs. 12c

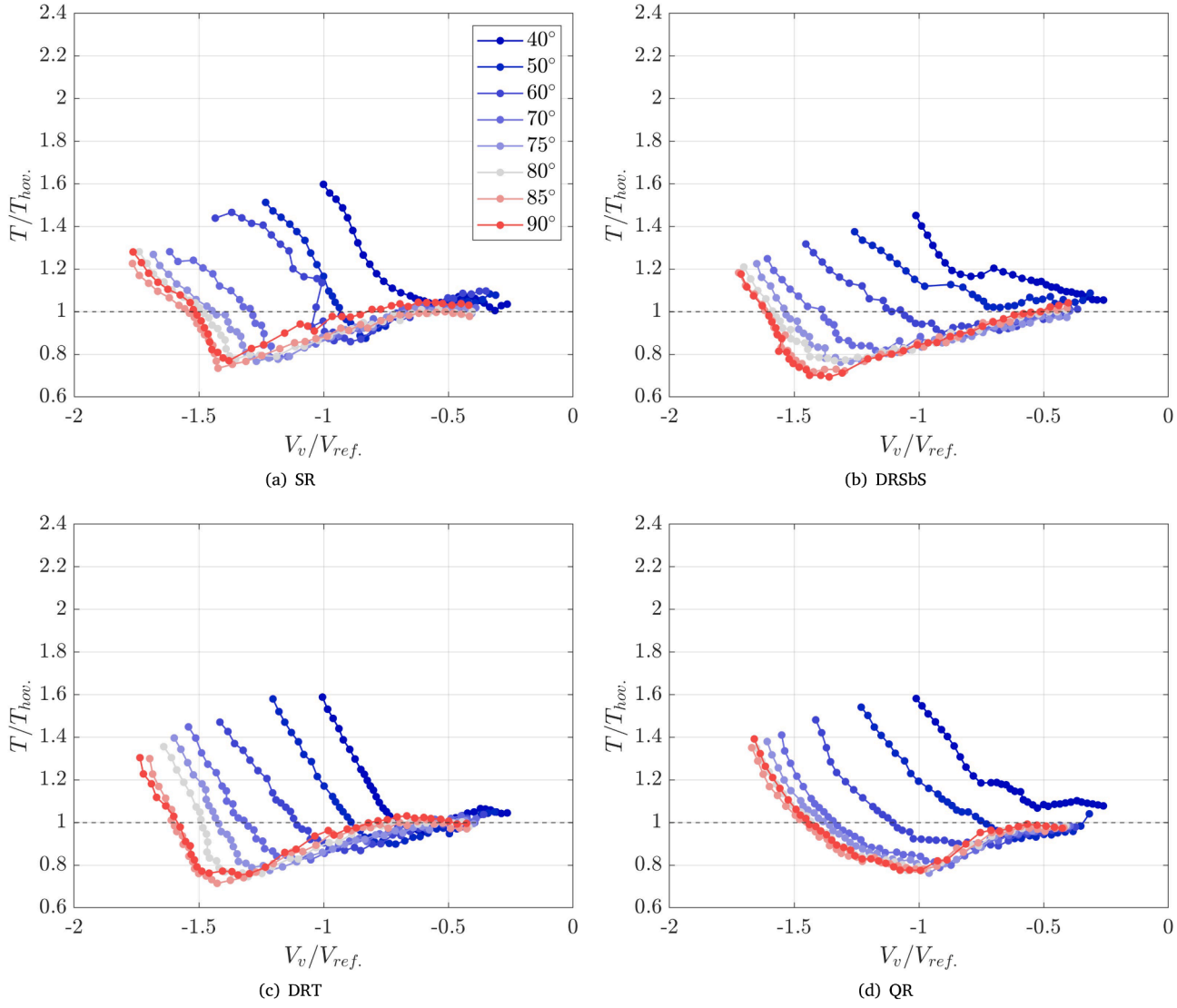
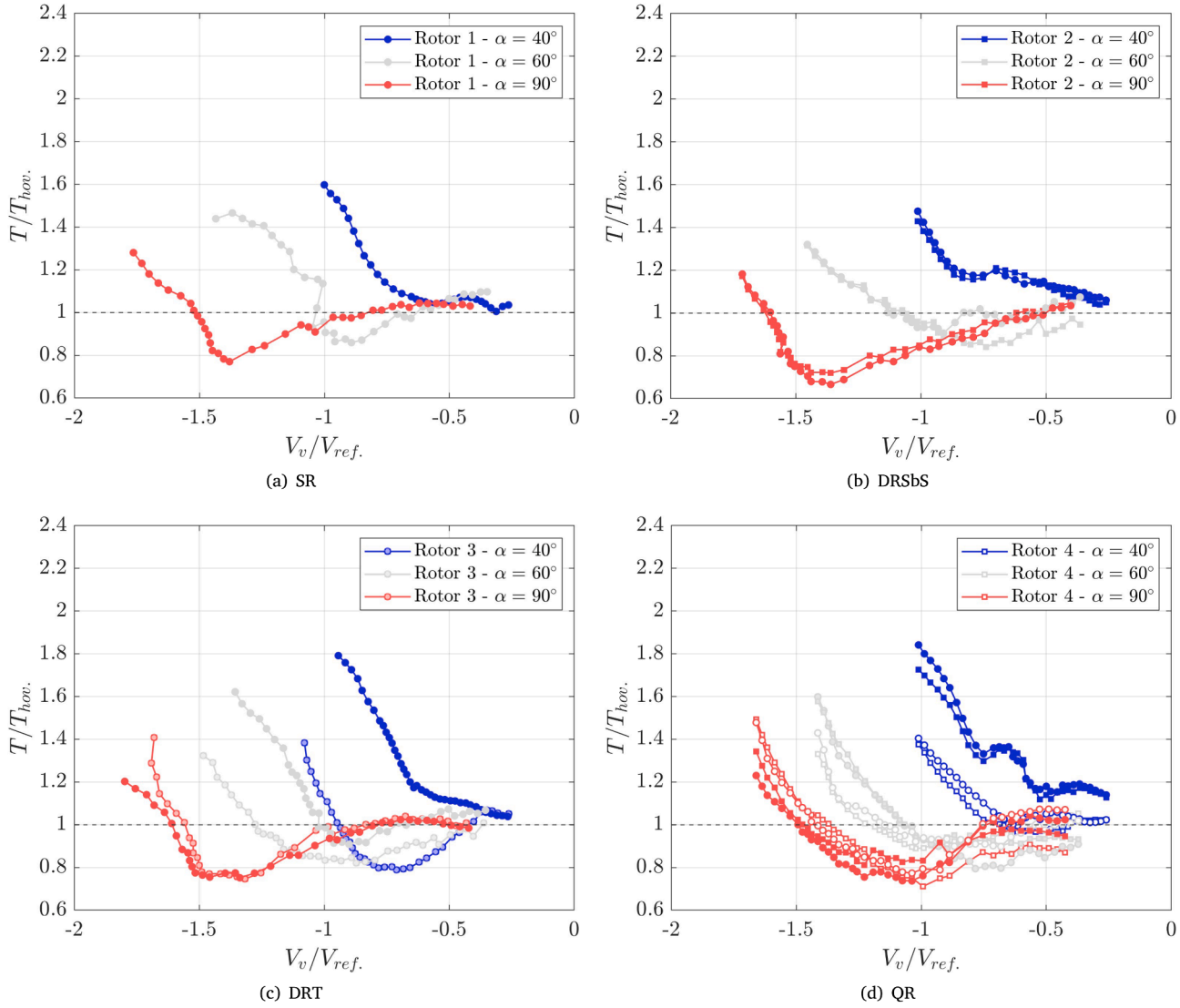


Fig. 11. Non-dimensional thrust plotted against descent velocities for different descent angles, (a) SR, (b) DRSbS, (c) DRT and (d) QR configurations.

and 12d, the decrease in α causes the gap between the front and rear rotors to grow, whereas as $\alpha \to 90°$ similar thrust levels are re-established for all motors. On the other hand, for 12a and b, such a dependency on α is lost, with all rotors outputting comparable levels of thrust, whichever α.

It is important to underline, however, that this systematic difference in thrust between different rotors is obtained by averaging across a relatively large acquisition window of 30 s. Hence, caution is in order when evaluating Fig. 12. Significant unsteady instantaneous thrust fluctuations may still arise and disrupt the symmetry of the thrust levels, even for the DRSbS configuration or for the front (or rear) rotors of QR. Nonetheless, Fig. 12 provides insights into the effect of rotor placements within a multirotor configuration experiencing VRS. Given the restrictions associated with take-off and landing in urban environments, and the increased disc loading expected for eVTOLs [17], VRS could get closer to a rotorcraft's flight envelope; hence, defining more *VRS-resistant* configurations by design could help mitigate some of the shortcomings inherently associated with eVTOLs operating in descent flight.

Moving on to Fig. 13, the experimental data measured during the aerodynamic load campaign is presented in terms of the non-dimensional induced velocity, $V_i/V_{ref.}$, and non-dimensional required power, $V_v + V_i/V_{ref.}$, for the SR and QR configurations. Experimental data, plotted with circular markers, is presented alongside the analytical expressions obtained via momentum theory, shown with solid black lines in the range: $V_v/V_{ref.} \in [-3;-2] \cup [0;3]$. Non-dimensional induced velocity and required power distributions computed via momentum theory are also shown in the range $V_v/V_{ref.} \in [-2;0]$, with dashed black lines, where momentum theory is invalid. In addition, an existing experimental correlation is displayed with a thick solid line, Gordon [32]. Although the underlying hypotheses are not verified, momentum theory still offers reasonable results for low descent velocities in the range $V_v/V_{ref.} \in [-1;0]$. As shown in subplots 13a and c, data from Gordon [32] and the current experimental campaign show good agreement. Moving on to subplots 13b and d, data for the QR configuration is presented. Deviations from the literature can be noted for both the induced velocity and required power distributions; the markers appear shifted towards the right, and, consequently, peak induced velocity and required power are reached earlier and with steeper gradients in vertical velocity. In addition, both the maximum induced velocity and required power, which are measured for $\alpha = 90°$, grow slightly moving from the SR to the QR configuration, increasing from $V_i/V_{ref.} \simeq 3.50$ at $V_v/V_{ref.} \simeq -1.22$ to $V_i/V_{ref.} \simeq 3.75$ at $V_v/V_{ref.} \simeq -1.10$. Similarly, peak required power goes from $V_v + V_i/V_{ref.} \simeq 1.98$ at $V_v/V_{ref.} \simeq -1.22$ to $V_v + V_i/V_{ref.} \simeq 2.29$ at $V_v/V_{ref.} \simeq -1.10$. Data measured for shallower descent angles shows increasingly lower values of induced ve-



(a) SR (b) DRSbS (c) DRT (d) QR

Fig. 12. Non-dimensional thrust computed for individual rotors in the configuration, plotted against descent velocities for different descent angles, (a) SR, (b) DRSbS, (c) DRT and (d) QR configurations.

locity and required power, while also shifting towards higher descent velocities.

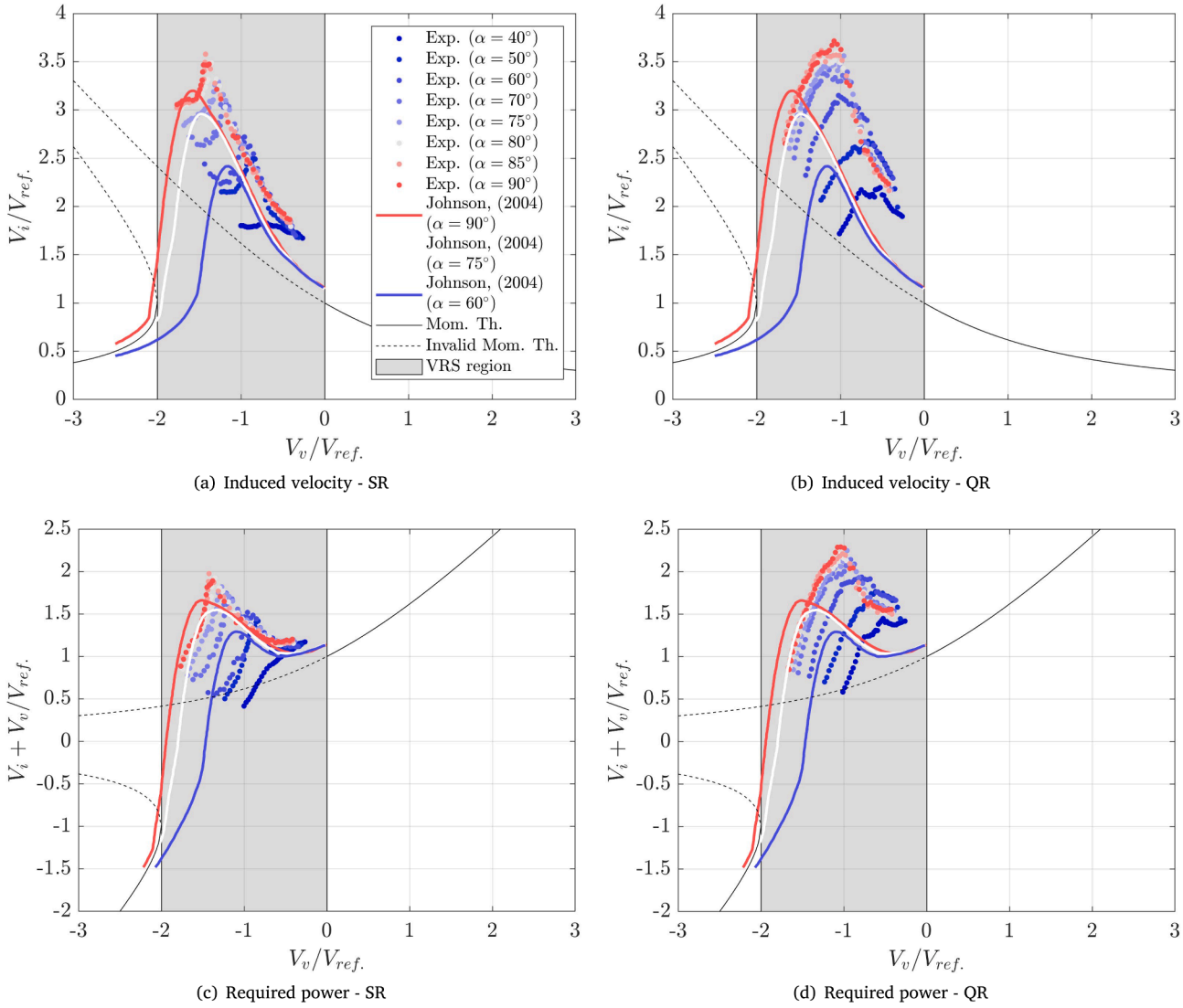
As thoroughly discussed by Johnson [11], the non-dimensional power distribution is a measure of the required power to generate a set level of thrust. In this sense, the negative correlation between vertical velocity and required power reveals the unstable nature of flight the VRS region: as an air vehicle happens to fly within the unstable portion of the $V_v + V_i/V_{ref.} - V_v$ plane, an increase in descent rate causes an increase in power required to generate the same thrust level. If not counteracted, the described condition can induce a further increase in descent rate, which, in turn, further increases the required power for a given thrust level. Thus, comparing Fig. 13c and d, one can deduce that moving from the SR to QR, the configurational effect increases the slope of the unstable region, thus amplifying the unstable positive feedback between descent rates and required power.

4.2. Flow fields

As previously discussed in the introduction to this paper, the flow field around a rotor in VRS undergoes a major topology modification compared to the hover condition. This section aims to quantitatively measure the aforementioned flow field modifications by comparatively analysing the S-PIV data for varying velocities and descent angles. For the sake of conciseness, the analysis has been limited to the SR and QR configurations.

To improve the readability of the figures showing the S-PIV flow fields, the absolute value of the descent velocity will be reported. Accordingly, an increase in the magnitude of the descent velocity may be described more concisely as an increase in descent velocity.

Firstly, the reader is referred to Fig. 14, where time-averaged flow fields around the SR configuration, at a descent angle of $\alpha = 90°$, are presented through non-dimensionalised velocity magnitude contours with streamlines superimposed. Velocity magnitude is computed using all three velocity components measured through S-PIV: U, V and W, the streamwise, spanwise and out-of-plane components, respectively. Velocity has been non-dimensionalised via the tip speed, $V_{tip} = \Omega R$. Fig. 14 shows six different subplots displaying flow fields for decreasing descent velocities. Each subplot is accompanied by an annotation on the right, indicating the absolute value of the non-dimensional descent velocity, which utilises $V_{ref.}$ as the velocity scale, computed for each configuration based on the generated thrust, using Eq. (1). Each subplot also features an annotation on the top, which indicates the mean thrust variation over the hover case and the descent angle. In addition, a sketch



(a) Induced velocity - SR

(b) Induced velocity - QR

(c) Required power - SR

(d) Required power - QR

Fig. 13. Non-dimensional induced velocity (top) and required power (bottom) for the SR and QR configurations, from current experimental data (•,•), momentum theory (——), invalid momentum theory (⋯⋯), VRS model from Johnson [11] (—,—).

of the rotor is shown for geometrical reference. Starting with the subplot in the top left corner, it shows the flow field generated by a rotor in hover: two distinct jets generated by the rotor blades can be identified, although these quickly coalesce into a single structure as early as $X/R = 0.5$.

Increasing the descent velocity from $|U_\infty/V_{ref.}| = 0$ to $|U_\infty/V_{ref.}| = 0.53$, leads to the subplot in the top right corner: only subtle variations with the hover case can be identified, as predicted by momentum theory, which still holds for small descent velocities. Similarly, a negligible variation in thrust is observed, with a 4% increase over the hover case. The flow field is still dominated by the jet-like structure issued from the rotor; however, a slight reduction in the induced velocity generated in the wake can be observed, alongside a premature divergence of the wake. Large recirculation regions start to appear on both sides of the rotor wake. A further increase in the descent velocity, from $|U_\infty/V_{ref.}| = 0.53$ to $|U_\infty/V_{ref.}| = 0.84$, intensifies these trends. The flow field shown in the subplot in the middle row on the left essentially shows the same flow topology, although the mentioned modifications are more pronounced. The velocity in the wake is more significantly reduced, the wake diverges more, and the recirculation regions have moved upwards, towards the rotor plane. Further increase in descent velocity to $|U_\infty/V_{ref.}| = 1.2$, leads to the subplot in the middle row, on the right. Two flow structures now coexist in the region of interest: the centres of the recirculation regions have come into view, showing the ring vortex almost in its entirety, while the jet issuing from the rotor is even more spread out, reaching a lower velocity. These flow modifications lead to a 8% thrust reduction over the hover case. The last row of subplots shows the flow fields achieved for the highest descent velocities, $|U_\infty/V_{ref.}| = 1.42$, on the left, and $|U_\infty/V_{ref.}| = 1.57$, on the right. A descent velocity of $|U_\infty/V_{ref.}| = 1.42$ causes the ring vortex to be pushed closer to the rotor plane, where its effect on the rotor performance is stronger, causing a 13% thrust loss over the hover case.

Simultaneously, the presence of the mentioned ring vortex prevents the wake of the rotor from developing, and a major velocity reduction can be observed in the wake. Finally, moving to $|U_\infty/V_{ref.}| = 1.57$, the ring vortex has partially left the region of interest, by shifting upwards. In this configuration, the effect of the ring vortex on the rotor performance is even more severe: a 21% reduction in thrust is observed. At this descent rate, the effects of the incoming dynamic pressure on the wake of the rotor are so strong that the downwash generated by the rotor blades barely develops, immediately diverging in the radial direction. The mentioned repositioning of the ring vortex across the rotor plane reveals a stagnation point, which marks the lower boundary of the vortex ring. Once the behaviour of the SR configuration in vertical

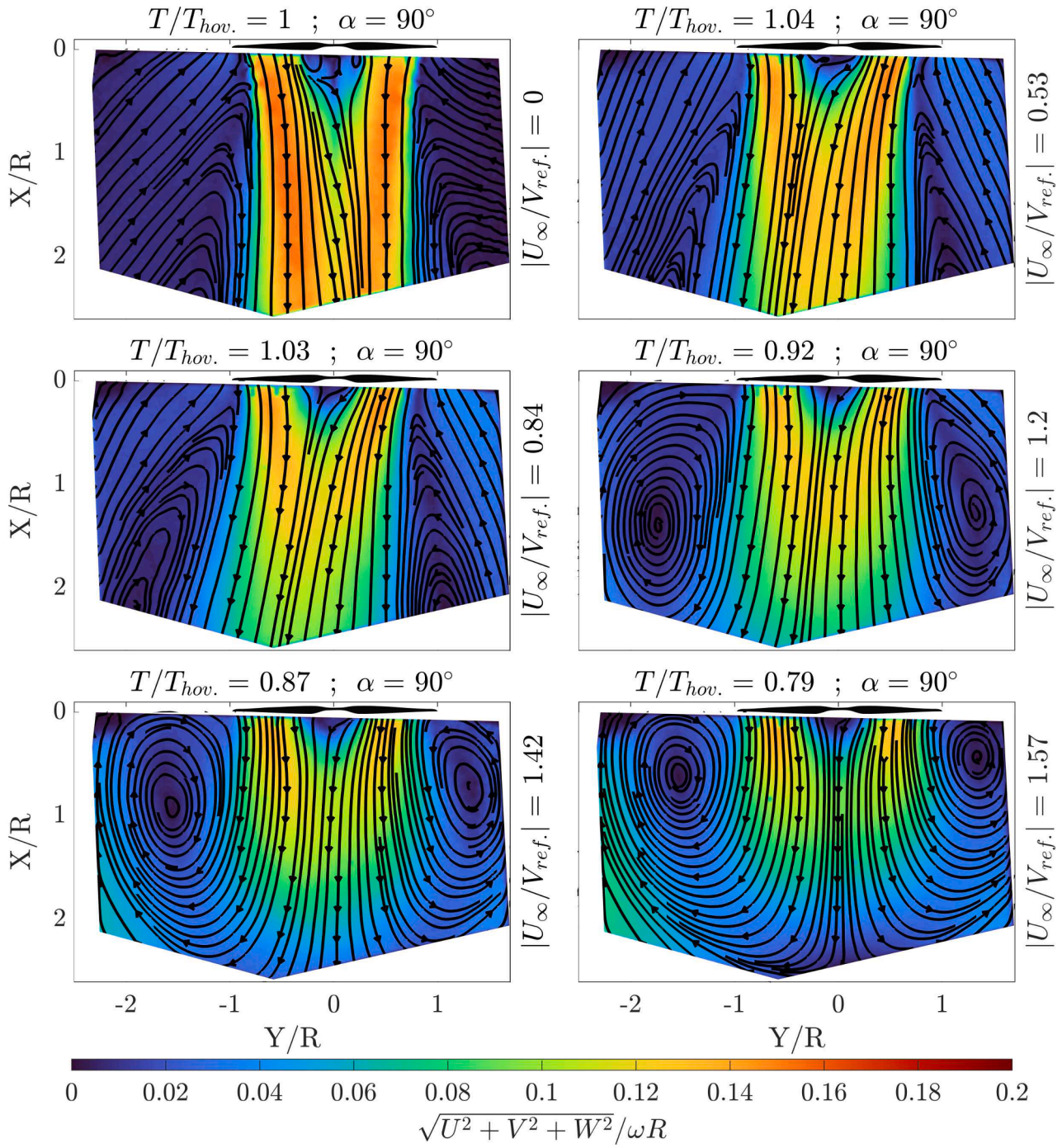


Fig. 14. Time averaged S-PIV flow fields displayed as non-dimensional velocity magnitude contours with streamlines superimposed for the SR configuration, $\alpha = 90°$ and multiple descent velocities.

descent ($\alpha = 90°$) has been discussed for different descent velocities, the effect of α is investigated, as in Fig. 15.

The flow fields generated by the SR configuration at the two highest descent velocities are compared for $\alpha \in [60°, 70°, 80°]$. As $\alpha \neq 90°$, two velocity components make up the overall translational velocity, as presented in the decomposition shown in Eq. (2) and (3). For the sake of simplicity, U_∞ has been taken as a reference value for different descent conditions, as it represents the wind tunnel operating condition. For these reasons, care needs to be taken while comparing different descent angles for equal $|U_\infty/V_{ref.}|$ values. For these reasons, Table 1 provides an overview of the V_v and V_h values obtained for different descent angles.

Firstly, the reader is referred to the first row of Fig. 15, where $\alpha = 80°$ is considered. To correctly interpret the flow structure visible in Fig. 15, it is important to recall that the relative position of the rotor plane and the cameras does not change with different α: this implies that the rotor plane is always positioned at $X/R = 0$. In other words, the S-PIV data is shown in the reference frame of the device, with the incoming flow from the wind tunnel changing direction according to α. Starting with the first column on the left, flow fields measured at $|U_\infty/V_{ref.}| \simeq 1.30$ and different descent angles are displayed. Decreasing α, *i.e.* moving from top to bottom of Fig. 15, causes the ring vortex to tilt in the $X/R - Y/R$ plane. Such rotation also introduces an asymmetry in the vortex ring structure: the front side of the structure gets

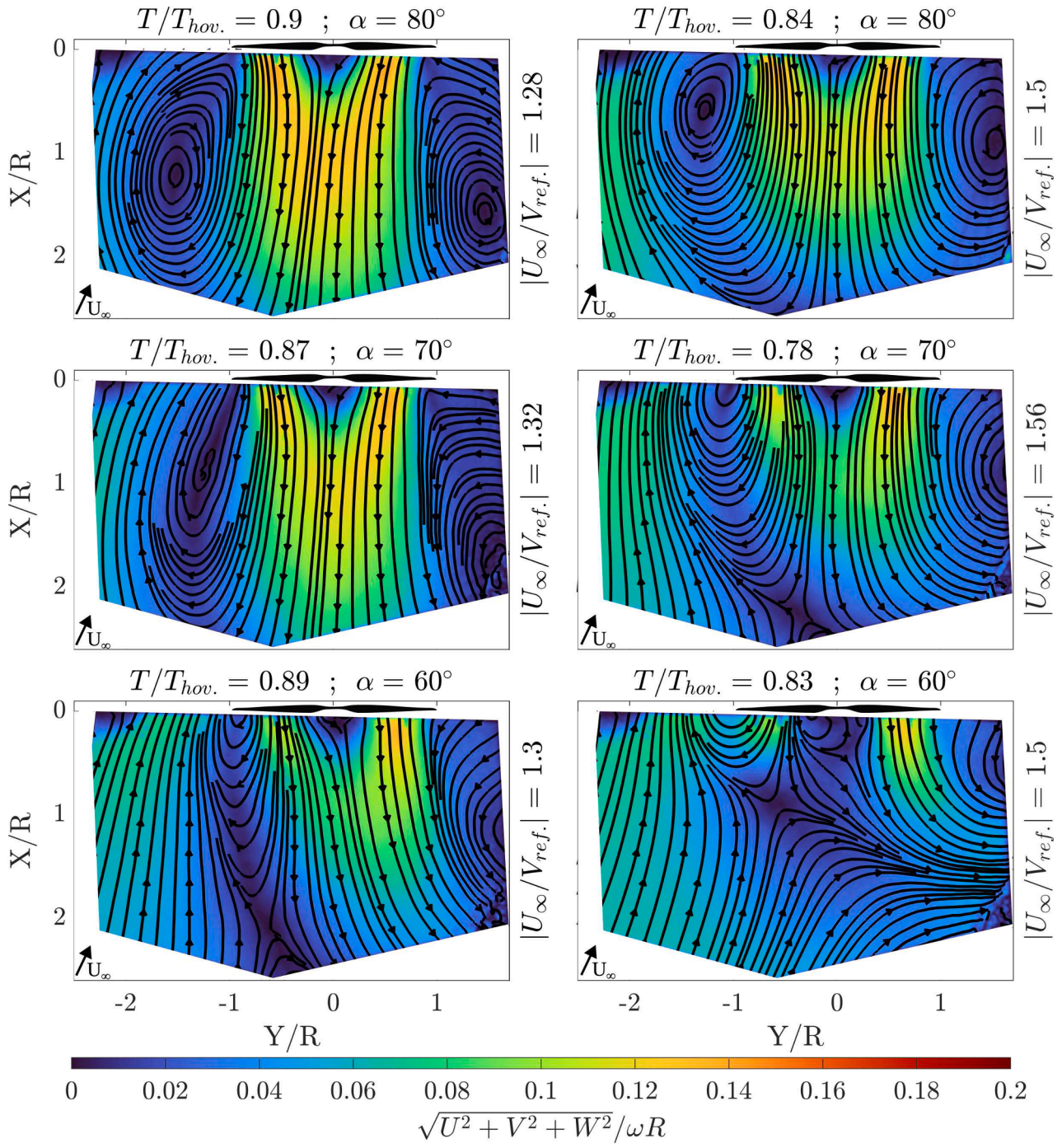


Fig. 15. Time averaged S-PIV flow fields displayed as non-dimensional velocity magnitude contours with streamlines superimposed for the SR configuration, $\alpha \in [60°, 70°, 80°]$ and multiple descent velocities.

smaller and is pushed towards the rotor plane, while the rear side is pushed away from the rotor plane and stretches further in the Y/R direction.

Increasing the descent velocity causes the vortex ring to be pushed against the rotor plane, which, in turn, affects the development of the rotor downwash underneath the rotor; a similar effect is caused by the approach of the ring vortex towards the rotor plane, due to a decrease in α. As α decreases, the downwash from the front rotor blade is suppressed, while the one generated by the rear blade is preserved.

In addition, for $\alpha = 60°$, shown in the bottom left corner of Fig. 15, the stagnation point is visible, located at roughly $X/R \simeq 2$ and $Y/R \simeq -0.5$. This velocity contour proves that the stagnation point moves along the boundary of the vortex ring as the descent angle changes.

As the descent velocity is increased from $|U_\infty/V_{ref.}| \simeq 1.3$ to $|U_\infty/V_{ref.}| \simeq 1.5$, the flow field topology changes significantly, as shown in the right column of Fig. 15. Starting with the flow field in the top right corner ($\alpha = 80°$), and comparing it with the flow field on the left, the increase in descent velocity causes the stagnation point to come barely into view in the ROI, as it is pushed towards the rotor plane. As per the previous descent rate, the vortex ring around the rotor plane appears rotated in the $X/R - Y/R$ plane, according to α.

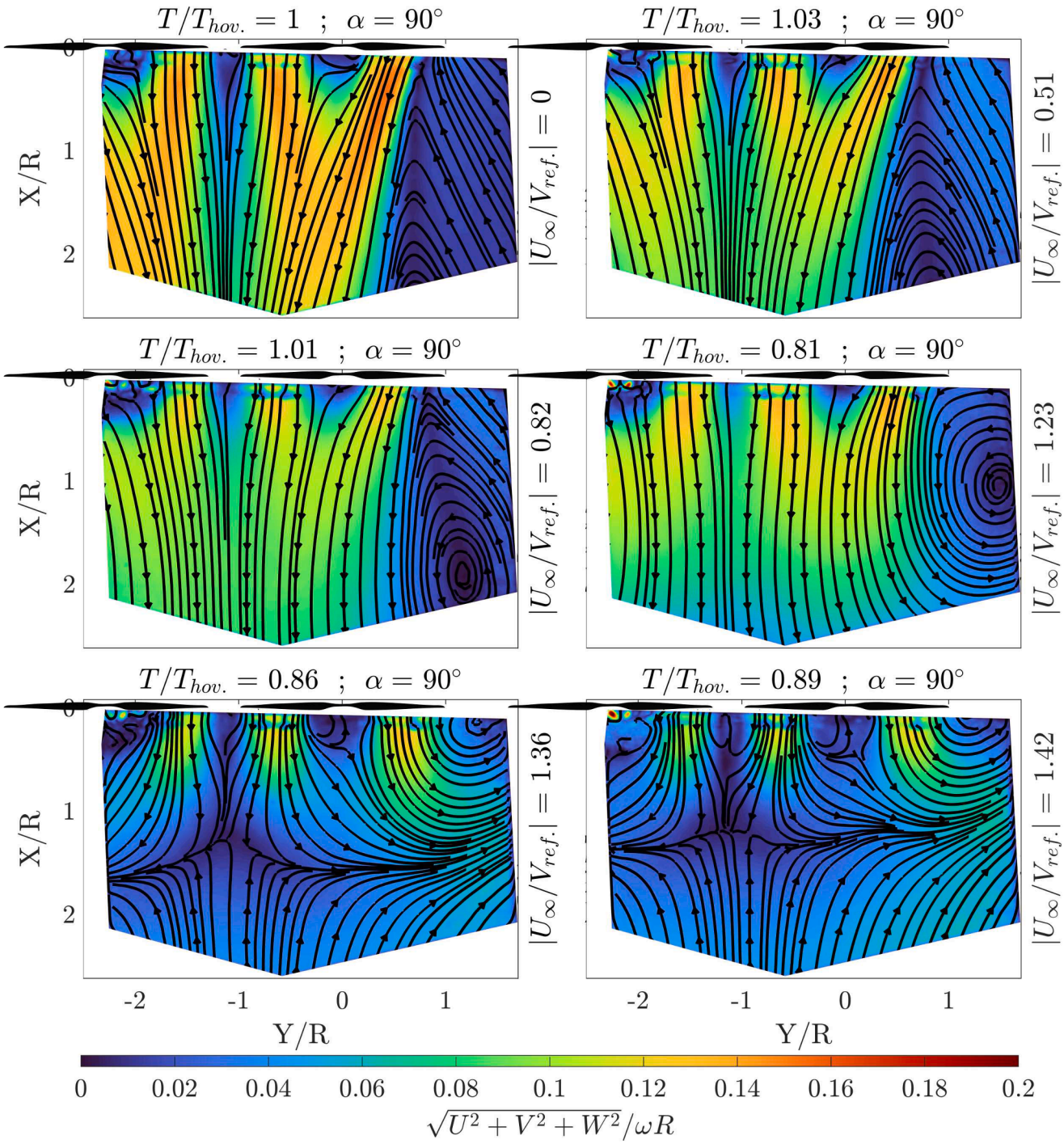


Fig. 16. Time averaged S-PIV flow fields displayed in the eROI as non-dimensional velocity magnitude contours with streamlines superimposed for the QR configuration, $\alpha = 90°$ and multiple descent velocities.

Table 1
Overview of the translational velocity decomposition for different descent angles.

	$\lvert V_v/V_{ref.}\rvert$	$\lvert V_h/V_{ref.}\rvert$	$\lvert U_\infty/V_{ref.}\rvert$
$\alpha = 80°$	1.284	0.203	1.30
$\alpha = 70°$	1.236	0.402	1.30
$\alpha = 60°$	1.158	0.590	1.30
$\alpha = 80°$	1.482	0.235	1.50
$\alpha = 70°$	1.427	0.464	1.50
$\alpha = 60°$	1.337	0.681	1.50

Decreasing the descent angle to $\alpha = 70°$, causes the stagnation point to move upwards even further. One could argue that the flow topology is progressively shifting towards the TWS regime, with the recirculating regions mostly developing above the rotor plane, especially for the front blades. The stagnation point has shifted towards the front blade. A further decrease in descent angle, to $\alpha = 60°$, leads to the flow field presented in the bottom right tile of Fig. 15. The stagnation region has now markedly shifted towards the front blade, and the recirculation regions are barely visible within the ROI, indicating that the evolution from the VRS to the TWS regime is further progressing. Moving along the columns of Fig. 15 isolates the effect of α on $T/T_{hov.}$ for a given

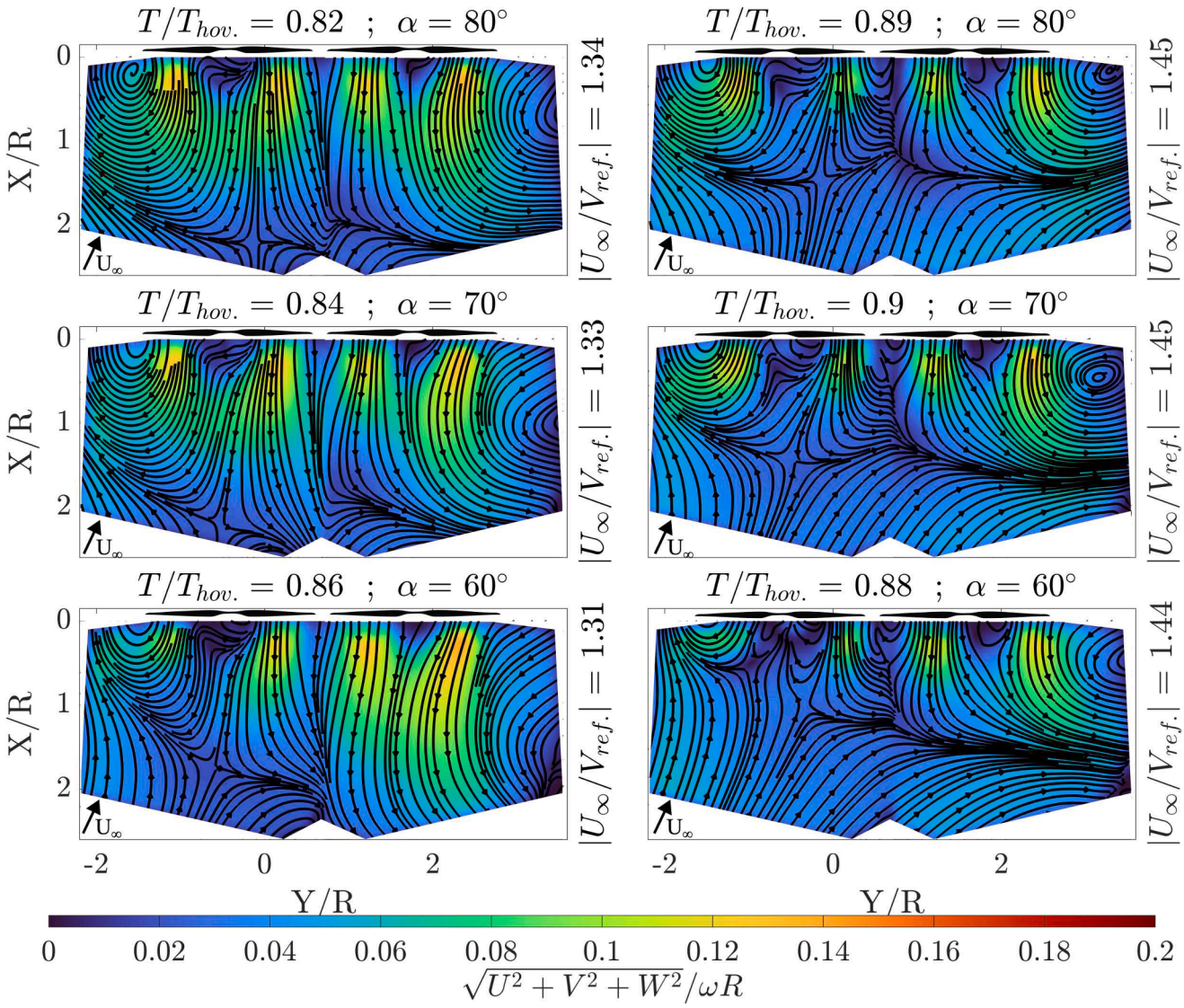


Fig. 17. Time averaged S-PIV flow fields displayed in the eROI as non-dimensional velocity magnitude contours with streamlines superimposed for the QR configuration, $\alpha \in [60°, 70°, 80°]$ and multiple descent velocities.

descent velocity: as α is reduced, thrust is progressively restored, increasing from $T/T_{hov.} = 0.87$ at $\alpha = 80°$ to $T/T_{hov.} = 0.89$ at $\alpha = 60°$ for $|U_\infty/V_{ref.}| \simeq 1.34$. A similar behaviour can be observed for the higher descent velocity of $|U_\infty/V_{ref.}| \simeq 1.5$, displayed in the column on the right. Moving on to the QR configuration, the S-PIV flow fields are shown in Fig. 16 for similar descent velocities as in Fig. 14. Before addressing each flow field individually, it can be noted that for the current rotor separation distance, a single vortex ring structure wraps around the device. Veismann et al. [18] conducted a parametric study on separation distance for rotors in axial descent and found similar results, proving that for separation distances small enough, close to $d/D \simeq 1$, the ring vortices generated by each rotor merge, forming a large unified structure around the multirotor configuration. As per the SR configuration, the progressive increase of the descent velocity causes the rotor wakes to collapse, diverging prematurely. Simultaneously, two recirculation regions form around the device and progressively shift towards the rotor plane for decreasing descent velocities. Although the flow fields are displayed only partly, as they extend further outside the FOV, overall symmetry is observed for all descent velocities. Comparing the SR (Fig. 14) and QR configurations in terms of thrust, a major difference arises, noting that the minimum thrust within the selected descent velocities, is measured for $|U_\infty/V_{ref.}| = 1.23$, with the centre of the recirculation region positioned roughly at $X/R \simeq 1$. On the contrary, the minimum thrust for the SR configuration is reached at $|U_\infty/V_{ref.}| = 1.57$, with the centres of the recirculating regions roughly positioned at $X/R \simeq 0.5$. While the shift of the minimum thrust towards higher descent velocities has already been commented on during the discussion of Figs. 9 and 11, here it appears as if the minimum thrust is generated when the recirculation regions are located at a rather constant distance from the rotor plane, which is equal to roughly half the device's characteristic length, *i.e.* one rotor radius for the SR and two rotor radii for the QR configuration. Indeed while thrust is almost constant at roughly $T/T_{hov.} \simeq 1$ for $|U_\infty/V_{ref.}| \in [0, 0.82]$ a sudden drop to $T/T_{hov.} = 0.81$ is observed at $|U_\infty/V_{ref.}| = 1.23$. From this point on, as the descent velocity is further increased, thrust increases, reaching $T/T_{hov.} = 0.89$ for $|U_\infty/V_{ref.}| = 1.42$, as the configuration progressively shifts towards the TWS state. Consistently, the centre of the recirculation region moves upwards, progressively leaving the ROI.

Fig. 17 reports on the effect of the descent angle on the flow field around the QR configuration for $|U_\infty/V_{ref.}| \in [1.34, 1.45]$ and $\alpha \in [60°, 70°, 80°]$.

Starting with the first column of Fig. 17, the effect of different descent angles on the flow field topology is presented for $|U_\infty/V_{ref.}| \simeq 1.34$.

As described for the SR configuration, decreasing the descent angle causes the vortex ring to rotate in the $X/R - Y/R$ plane. The rotation of the vortex ring structure can be appreciated by noting the change in location of the recirculation regions at the front and back of the device: as the recirculation regions rotate in the $X/R - Y/R$ plane, they induce an asymmetry in the flow field generated by the front and rear rotors. Such an asymmetry is even more pronounced for $\alpha = 60°$, as the recirculation region has mostly shifted above the rotation plane for the front rotor, almost completely suppressing the development of the wake underneath the rotor. On the contrary, the reduction in α causes the rear recirculation region to shift further away from the rotor plane, allowing the rotor wake to develop underneath it. As the descent angle is reduced, thrust is progressively restored, increasing from $T/T_{hov.} = 0.82$ at $\alpha = 80°$ to $T/T_{hov.} = 0.86$ at $\alpha = 60°$ for $|U_\infty/V_{ref.}| \simeq 1.3$. However, recalling the thrust data presented in Fig. 12, as the descent angle is reduced, front and rear rotors start behaving differently, with the latter generating lower thrust. This is also consistent with the correlation between the position of the centre of the recirculation region and the thrust level, with the rear rotor showing a more developed wake, while developing less thrust than the front rotor, whose wake is suppressed and rapidly rotates upwards, developing mostly above the rotor plane.

As the descent velocity is increased, the rotor wakes appear closer to the rotor plane, while also developing significantly less than for $|U_\infty/V_{ref.}| \simeq 1.3$. Indeed, the QR has already surpassed the condition of minimum thrust, as indicated by the thrust levels annotated on the subplots and further confirmed by the positioning of the recirculation regions. In this condition, thrust for QR is restored more slowly than for the other configurations, as indicated in Fig. 11. Also, the effect of α is less pronounced, hence $T/T_{hov.}$ is rather constant for $|U_\infty/V_{ref.}| = 1.45$, independently of α.

5. Conclusion

The VRS phenomenon for multicopters has been the subject of an experimental investigation conducted in the Rotor Test Facility Göttingen (RTG) of the German Aerospace Centre (DLR), with a focus on understanding its aerodynamic characteristics through thrust and power measurements, complemented by S-PIV measurements. These measurements were conducted for multiple descent rates in the range $U_\infty/V_{ref.} \in [-1.7; 0]$ and for multiple descent angles, with $\alpha \in [40; 90°]$. Four configurations were comparatively assessed: the single rotor is used as the reference configuration, while the dual rotors in side-by-side and tandem configurations, and the quadrotor configuration are tested to investigate the interactional effects.

The aerodynamic load campaign indicated that the tested multirotor platforms exhibit significant configurational effects. These effects have been quantified by investigating the evolution of thrust, thrust fluctuations, non-dimensional induced velocity and required power.

The analysis of thrust fluctuations, which are a measure of the thrust-induced vibrations, revealed that while DRSbS exhibits a thrust fluctuation profile that is very similar to the baseline SR configuration, arranging the dual rotors in a tandem configuration (DRT) causes the RMS of the thrust signal to increase by roughly 30%. A further increase is found for the QR configuration, which experiences a doubling of the thrust fluctuations compared to the SR configuration. In addition, for the QR configuration, the RMS distribution exhibits a more distinct peak, which is located at a higher descent velocity than for other configurations.

A similar pattern was also observed for the mean thrust reduction: the SR and DRSbS configurations exhibit very similar thrust levels, with a quasi-linear reduction of T/Th with decreasing descent velocities leading to minimum thrust levels equal to $T/T_{hov.} = 0.72$ for $V_v/V_{ref.} \simeq -1.42$ and to $T/T_{hov.} = 0.7$ for $V_v/V_{ref.} \simeq -1.36$, for the SR and DRSbS configurations, respectively. Instead, the DRT configuration shows a non-linear reduction in thrust, at least for larger descent angles. The linearity is restored as α is reduced. Nonetheless, the DRT configuration achieves a minimum thrust of $T/T_{hov.} = 0.74$ for the same descent velocity. The QR configuration, instead, experiences a slightly higher minimum thrust of $T/T_{hov.} = 0.78$ for a significantly larger descent velocity value of $V_v/V_{ref.} \simeq -0.99$. In addition, as the descent velocity is reduced, thrust is restored more slowly. The thrust levels experienced by the different rotors provide useful information on the effect of rotor placement within the configuration, as the rear rotors systematically generate lower thrust than the front ones for small descent angles.

The analysis of the FPP scatter plot revealed that the QR experiences a significant shift of the *deep* VRS region to higher descent velocities and smaller descent angles, together with the extension of the shallow VRS region in the same direction shared with all multirotor configurations. Given the non-dimensional nature of the FPP plot presented in the current work, the configurational effects presented herein should also be accompanied by considerations regarding the increase in disc loading and its effect on the dimensional representation of the FPP plot, as indicated by Brown [17].

The evaluation of the configurations' non-dimensional required power revealed that the inherent instability of flight in the VRS regime is exacerbated for the QR configuration. A stronger gradient in the required power/descent velocity plane is shown, indicating a stronger positive feedback between reduction in descent velocity and increase in required power for a set level of thrust.

The S-PIV campaign clarified the evolution of the flow field topology in VRS for the SR and QR configurations, for multiple descent velocities and descent angles.

As expected, the rotor wakes progressively break down as the absolute value of the descent velocity is increased. Large recirculation regions form around the configuration, and the rotor wakes start to rotate upwards, while producing lower induced velocity values. The occurrence of the minimum thrust is found to correlate well with the position of the recirculating regions: with the SR and QR configuration generating the least thrust when the centres of the recirculation regions are located roughly at half of the configuration's characteristic length from the rotor plane.

The analysis of the flow fields at multiple descent angles, revealed that decreasing α causes the ring vortex to rotate in the $X/R - Y/R$ plane and to deform: the ring vortex at the front of the device is reduced in size and pushed towards the rotor plane, while, on the contrary, the side of the vortex ring located at the back is enlarged and pushed away from the rotor plane. The velocimetry data also revealed good correlation with the load data, confirming the asymmetry between the front and rear rotors in the QR configuration.

Future work will focus on further extending the analysis of the S-PIV data, including all configurations and additional combinations of descent velocity and descent angles, which have not been reported herein for the sake of conciseness.

CRediT authorship contribution statement

Giosuè Longobardo: Writing – review & editing, Writing – original draft, Visualization, Software, Methodology, Investigation, Formal analysis, Data curation, Conceptualization; **Alexander Heintz:** Writing – review & editing, Software; **Johannes Braukmann:** Writing – review & editing, Validation, Supervision, Methodology, Conceptualization; **C. Christian Wolf:** Writing – review & editing, Validation, Supervision, Methodology, Conceptualization; **Jochen Raddatz:** Writing – review & editing, Validation, Software; **Tommaso Astarita:** Writing – review & editing, Validation, Supervision, Funding acquisition; **Fabrizio De Gregorio:** Writing – review & editing, Validation, Supervision, Funding acquisition; **Anthony D. Gardner:** Writing – review & editing, Validation, Supervision, Resources, Project administration, Methodology, Investigation, Funding acquisition, Conceptualization; **Markus Raffel:** Writing – review & editing, Supervision, Resources, Methodology, Funding acquisition.

Funding

This research was funded by the DLR Project ROME and carried out in the scope of the GARTEUR AG28: Vortex Ring State.

Declaration of competing interest

The authors declare that they have no known competing financial interests or personal relationships that could have appeared to influence the work reported in this paper.

Acknowledgements

The authors wish to thank Mr M. Krebs for contributing to the realisation of the experimental setup.

Data availability

Data will be made available on request.

Appendix A. Normalisation of loads data

As discussed in Section 3, in the current work, the experimental campaign has been conducted by setting a fixed rotation rate of 80 Hz for every descent velocity. However, this is not the standard procedure for rotor loads experimental campaigns, which are usually performed under trimmed-thrust conditions. To account for this, the current data has been non-dimensionalised using a variable reference velocity, $V_{ref.}$, which is computed using the measured thrust. This led to the inhomogeneous scatter of the measurement points of Fig. 9.

Another possible approach would be to set a fixed reference velocity, computed with the thrust measured in hover conditions: $V_{hov.} = \sqrt{T_{hov.}/2\rho A}$. This leads to a modified FPP plane, as shown in Fig. A.1.

Interestingly, comparison of 9a and A.1 reveals that the location and extent of the VRS regions remain essentially unchanged in size and location, apart from a slight shift towards higher descent velocity values. While the overall distribution is modified, with $V_h/V_{hov.}$ and $V_v/V_{hov.}$ attaining lower values, both normalisation approaches provide similar results for VRS characterisation.

Fig. A.2 allows for a more direct comparison of the effects of using different scaling velocities: as previously introduced, using $V_{ref.}$ leads to an inhomogeneous scattering of the data. As $T/T_{hov.} > 1$, then $|V_v/V_{hov.}| > |V_v/V_{ref.}|$. Conversely, for $T/T_{hov.} < 1$, $|V_v/V_{hov.}| < |V_v/V_{ref.}|$. The largest difference between the two approaches is found for high non-dimensional velocities in absolute value, where up to a 50% increase in thrust over the hover case is measured.

As a consequence, minimum thrust is slightly anticipated when using $V_{hov.}$ compared to $V_{ref.}$, with an offset of about 0.17 between the two different normalisations.

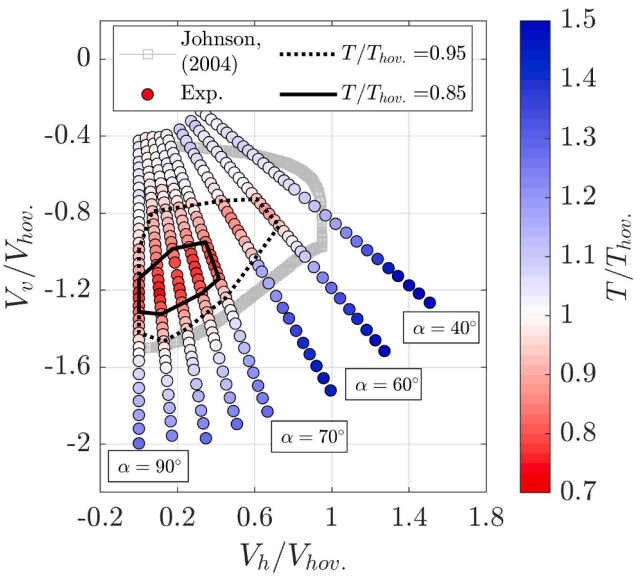


Fig. A.1. Variation on the FPP plane scatter plot for the SR configuration using $V_{hov.}$ as the reference velocity.

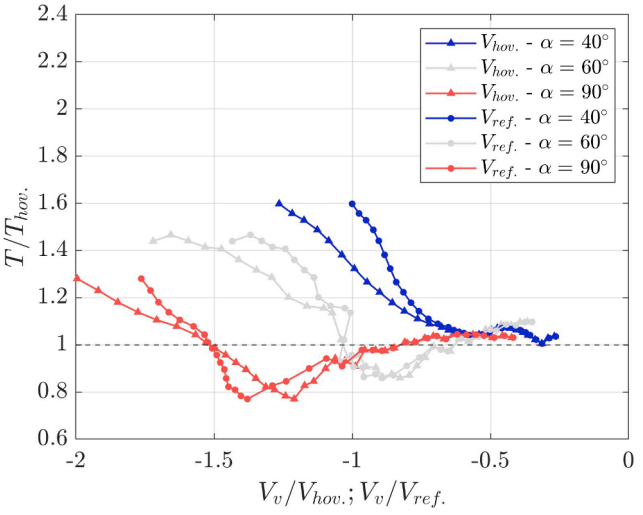


Fig. A.2. Comparison of the FPP plot for the SR configuration using different reference velocities.

References

[1] M. Veismann, D. Yos, M. Gharib, Parametric study of small-scale rotors in axial descent, Phys. Fluids 34 (3) (2022) 035124. https://doi.org/10.1063/5.0083761

[2] J.P. Reeder, F.B. Gustafson, On the Flying Qualities of Helicopters, Technical Report TN-1799, NATIONAL ADVISORY COMMITTEE FOR AERONAUTICS, 1949.

[3] J.M. Drees, W.P. Hendal, The field of flow through a helicopter rotor obtained from wind tunnel smoke tests, J. Aircr. Eng. 23 (266) (1950) 107–111.

[4] W.J. Castles, R.B. Gray, Empirical Relation Between Induced Velocity, Thrust, and Rate of Descent of a Helicopter Rotor as Determined by Wind-Tunnel Tests of Four Model Rotors, Technical Report TN-2474, NATIONAL ADVISORY COMMITTEE FOR AERONAUTICS, 1951.

[5] A. Gessow, Review of Information on Induced Flow of a Lifting Rotor, Technical Report TN-3238, NATIONAL ADVISORY COMMITTEE FOR AERONAUTICS, 1954.

[6] J.E. Yeates, Flight Measurements of the Vibration Experienced by a Tandem Helicopter in Transition, Vortex-Ring State, Landing, Approach, and Yawed Flight, Technical Report TN-4409, NATIONAL ADVISORY COMMITTEE FOR AERONAUTICS, 1958.

[7] P.F. Yaggy, K.W. Mort, Wind-Tunnel Tests of Two VTOL Propellers in Descent, Technical Report TN-1766, NATIONAL ADVISORY COMMITTEE FOR AERONAUTICS, 1962.

[8] K. Washizu, A. Azuma, J. Koo, T. Oka, Experimental study on the unsteady aerodynamics of a model helicopter rotor operating in the vortex ring state, in: Symposium on Structural Dynamics and Aeroelasticity, American Institute of Aeronautics and Astronautics, 1965. https://doi.org/10.2514/6.1965-1112

[9] A. Azuma, A. Obata, Induced flow variation of the helicopter rotor operating in the vortex ring state, J. Aircr. 5 (4) (1968) 381–386. https://doi.org/10.2514/3.43954

[10] M.D. Betzina, Tiltrotor descent aerodynamics: a small-scale experimental investigation of vortex ring state, in: Proceedings of the Vertical Flight Society Forum 57 - Washington, D.C. 2001, 2001.

[11] W. Johnson, Model for vortex ring state influence on rotorcraft flight dynamics, in: American Helicopter Society 2004, San Francisco, California, USA, 2004.

[12] P.M. Basset, C. Chen, J.V.R. Prasad, S. Kolb, Prediction of vortex ring state boundary of a helicopter in descending flight by simulation, J. Am. Helicopter Soc. 53 (2) (2008) 139–151. https://doi.org/10.4050/jahs.53.139

[13] J.T. Doo, M.A. Tsairides, M.D. Pavel, M. Smith, A. Didey, E. Bennet, C. Hange, M. Bromfield, N.P. Diller, J. Mooberry, NASA Electric Vertical Takeoff and Landing (eVTOL) Aircraft Technology for Public Services –A White Paper, Technical Report NAS/CR-20205000636, National Aeronautics and Space Administration, 2021.

[14] W. Johnson, C. Silva, E. Solis, Concept vehicles for VTOL air taxi operations, in: AHS Technical Conference on Aeromechanics Design for Transformative Vertical Flight, San Francisco, CA, 2018.

[15] G.P. Thomas Edwards, eVTOL Passenger Acceptance, Technical Report NASA/CR—2020–220460, National Aeronautics and Space Administration, 2020.

[16] EASA, Prototype Technical Design Specifications for Vertiports, Technical Report EASA.ED/2022/001, European Union Aviation Safety Agency, 2022.

[17] R. Brown, Are eVTOL aircraft inherently more susceptible to the vortex ring state than conventional helicopters?, in: 48th European Rotorcraft Forum, Winterthur, Switzerland, 2022. https://doi.org/10.4050/f-0079-2023-18068

[18] M. Veismann, C. Dougherty, M. Gharib, Effects of rotor separation on the axial descent performance of dual-rotor configurations, Flow 3 (2023). https://doi.org/10.1017/flo.2022.31

[19] S. Chae, S. Lee, J. Kim, Effects of rotor–rotor interaction on the wake characteristics of twin rotors in axial descent, J. Fluid Mech. 952 (2022) A31. https://doi.org/10.1017/jfm.2022.913

[20] R.B. Green, E.A. Gillies, R.E. Brown, The flow field around a rotor in axial descent, J. Fluid Mech. 534 (2005) 237–261. https://doi.org/10.1017/S0022112005004155

[21] A. Savino, A. Gianotti, G. Droandi, M. Kerho, A. Zanotti, Experimental investigation of vortex ring state in an eVTOL propeller, Aerosp. Sci. Technol. 165 (2025) 110475. https://doi.org/10.1016/j.ast.2025.110475

[22] R.E. Brown, S.J. Newman, F.J. Perry, J.G. Leishman, Blade twist effects on rotor behaviour in the vortex ring state, in: 28th European Rotorcraft Forum, Bristol, UK., 2002.

[23] G. Bucherelli, D. Granata, A. Savino, A. Zanotti, Experimental investigation of the vortex ring state for side-by-side propellers in descent flight, Phys. Fluids 38 (3) (2026) 035136. https://doi.org/10.1063/5.0311688

[24] F. Lößle, A. Kostek, C. Schwarz, R. Schmid, A. Gardner, M. Raffel, Aerodynamics of small rotors in hover and forward flight, in: 48th European Rotorcraft Forum, Winterthur, Switzerland, 2022.

[25] A. Kostek, F. Lößle, R. Wickersheim, M. Keßler, R. Boisard, G. Reboul, A. Visingardi, M. Barbarino, A. Gardner, Experimental investigation of UAV rotor aeroacoustics and aerodynamics with computational cross-validation, CEAS Aeronaut. J. 15 (2023). https://doi.org/10.1007/s13272-023-00680-z

[26] A. Kostek, J. Braukmann, F. Lößle, S. Miesner, A. Visingardi, R. Boisard, V. Riziotis, M. Keßler, A. Gardner, Experimental and computational investigation of aerodynamic interactions in quadrotor configurations, J. Am. Helicopter Soc. 69 (2024). https://doi.org/10.4050/JAHS.69.022009

[27] S. Newman, R. Brown, J. Perry, S. Lewis, M. Orchard, A. Modha, Comparative numerical and experimental investigations of the vortex ring phenomenon in rotorcraft, in: American Helicopter Society, 57TH Annual Forum, 2001.

[28] S. Newman, R. Brown, J. Perry, S. Lewis, M. Orchard, A. Modha, Predicting the onset of wake breakdown for rotors in descending flight, J. Am. Helicopter Soc. 48 (2003). https://doi.org/10.4050/JAHS.48.28

[29] J. Stack, F. Caradonna, O. Savas, Flow visualizations and extended thrust time histories of rotor vortex wakes in descent, J. Am. Helicopter Soc. 50 (2005) 279–288. https://doi.org/10.4050/1.3092864

[30] A. Talaeizadeh, H.N. Pishkenari, A. Alasty, Quadcopter fast pure descent maneuver avoiding vortex ring state using yaw-rate control scheme, IEEE Robot. Autom. Lett. 6 (2) (2021) 927–934. https://doi.org/10.1109/lra.2021.3052436

[31] W. Stewart, Helicopter Behaviour in the Vortex-Ring Conditions, Technical Report RM No. 3117, Aeronautical Research Committee, 1951.

[32] J. Gordon, Principles of Helicopter Aerodynamics, Cambridge University Press, 2005.